Journal of *Marine Science and Engineering*

MDPI

Article

Distributed Adaptive Fault-Tolerant Formation Control for Heterogeneous USV-AUV Swarms Based on Dynamic Event Triggering

Haitao Wang [1], Hanyi Wang [2] and Xuan Guo [2,*]

[1] Department of Electrical and Electronic Engineering, University of Manchester, Manchester M13 9PL, UK; haitao.wang-2@postgrad.manchester.ac.uk
[2] School of Information Engineering, Wuhan University of Technology, Wuhan 430062, China; why949whmath@163.com
* Correspondence: guoxuan@whut.edu.cn

Abstract

This paper addresses the cooperative formation control problem for a heterogeneous unmanned system composed of Unmanned Surface Vehicles (USVs) and Autonomous Underwater Vehicles (AUVs) under coexisting constraints of actuator faults, time-varying communication topology, and communication delay. First, a unified dynamic model is established under the Euler–Lagrange framework. Building on this, a novel distributed adaptive fault-tolerant control (DAFTC) framework is proposed. This framework integrates a Dynamic Event-Triggered Mechanism (DETM) to address communication bandwidth limitations, alongside an adaptive fault-tolerant strategy to enhance system robustness. The novelty lies in the cohesive integration of DETM for communication efficiency and adaptive laws for online fault compensation (both loss of effectiveness and bias), while rigorously handling communication delays via Lyapunov–Krasovskii analysis. It is proven via Lyapunov stability analysis that the proposed control protocol ensures all signals in the closed-loop system remain semi-globally uniformly ultimately bounded, with the formation tracking error converging to an adjustable compact set. Simulation results demonstrate the framework's effectiveness. Compared to periodic communication (0.1 s interval), the proposed DETM reduces the communication load by over 99.6%. Even when subjected to a 25% effectiveness fault and a 5 Nm bias fault, the root-mean-square (RMS) tracking error is maintained below 0.15 m, validating the system's high performance and robustness.

Keywords: USV-AUV collaboration; formation control; dynamic event triggering; communication delay; adaptive fault-tolerant control

Received: 9 October 2025
Revised: 31 October 2025
Accepted: 5 November 2025
Published: 7 November 2025

Citation: Wang, H.; Wang, H.; Guo, X. Distributed Adaptive Fault-Tolerant Formation Control for Heterogeneous USV-AUV Swarms Based on Dynamic Event Triggering. *J. Mar. Sci. Eng.* **2025**, *13*, 2116. https://doi.org/10.3390/jmse13112116

1. Introduction

In recent years, marine exploration and development have become a strategic high ground in global technological competition. As types of key unmanned marine equipment, Unmanned Surface Vehicles (USVs) and Autonomous Underwater Vehicles (AUVs) have demonstrated great potential in fields such as environmental monitoring, resource exploration, seabed mapping, and national defense security. However, a single type of unmanned platform often struggles to meet the demands of increasingly complex marine tasks. USVs are equipped with continuous energy supply, high-precision GPS positioning capability, and high-rate radio communication capability, but their operational range is limited to the water surface [1–4]; in contrast, AUVs can dive underwater to perform

delicate tasks, but they are constrained by limited endurance, navigation accuracy drift, and low-bandwidth, and high-latency underwater acoustic communication [5–8].

Integrating USVs and AUVs into a cross-domain cooperative heterogeneous unmanned system enables the complementation of advantages, greatly expanding the breadth and depth of marine operations [9–11]. In this system, USVs can serve as mobile base stations for AUVs, providing navigation correction, data relay, and energy replenishment; meanwhile, AUVs act as underwater extensions of USVs to perform underwater detection tasks. The key to realizing this cooperative function lies in precise cross-domain formation control, i.e., ensuring that the AUV swarm maintains a predefined time-varying geometric configuration relative to USVs.

Nevertheless, achieving robust cross-domain formation control for USV-AUV systems faces numerous challenges. First, the dynamic models of USVs and AUVs differ significantly: the former are mainly affected by wind, waves, and currents, while the latter must account for buoyancy, hydrodynamic forces, and more complex six-degrees-of-freedom (6-DOF) motion. Most existing research on multi-agent formation control focuses on homogeneous systems, while studies on heterogeneous systems with significant differences are relatively scarce. For example, Guo et al. [12] proposed a distributed fixed-time sliding mode formation control (FTSMFC) method for the formation control problem of Unmanned Aerial Vehicle (UAV)–Unmanned Ground Vehicle (UGV) heterogeneous systems under directed topology with external disturbances, providing important insights for cross-domain cooperative control. Zhu et al. [13] studied the formation and trajectory tracking problems of UAV-USV systems, constructing a distributed event-triggered adaptive model predictive control (DEAMPC) formation control method using information from neighboring vehicles. Wu et al. [14] explored the collaborative coverage path planning problem for UAVs, USVs, and AUVs. Hu et al. [11] proposed a novel predefined-time terminal sliding mode control (PTSMC) strategy for heterogeneous cooperative systems consisting of USVs and AUVs. Ref. [15] proposed a local dynamic predictive control framework to assist AUVs and USVs in performing target search tasks without prior information in unknown marine environments. Ref. [16] used nonlinear model predictive control to solve the distributed dynamic rendezvous control problem of AUV-USV heterogeneous joint systems in the presence of unknown external disturbances.

In addition, communication constraints are a bottleneck restricting the cooperative performance of USV-AUV systems. Cross-domain communication between the two relies on underwater acoustic channels, which have inherently significant time delays, limited bandwidth, and unstable connection quality. Traditional control methods based on periodic communication generate large amounts of redundant data, quickly depleting valuable communication resources. Therefore, Event-Triggered Control (ETC) has been widely studied as an effective solution [17–20]. ETC only enables communication when the system error exceeds a preset threshold, thereby significantly reducing the network load. However, the fixed threshold of traditional static ETC makes it difficult to adapt to the dynamic changes of system states. To achieve a better balance between communication and control performance, the Dynamic Event-Triggered Mechanism (DETM) has emerged. By introducing a dynamically changing threshold, DETM allows the communication strategy to adapt to the real-time needs of the system [21–24].

Meanwhile, the complexity and unpredictability of the marine environment make system uncertainties and actuator faults non-negligible issues. The hydrodynamic parameters of unmanned platforms are usually difficult to model accurately, and actuators such as propellers and rudders may experience faults such as effectiveness degradation (loss of effectiveness) or bias under harsh marine conditions. If not addressed, these faults may lead to degraded formation performance or system instability. Therefore, Adaptive

Fault-Tolerant Control (FTC) with fault diagnosis and active compensation capabilities is crucial for ensuring task reliability. In recent years, distributed FTC has been widely applied in multi-agent systems. Ref. [25] designed a distributed adaptive fault-tolerant controller (DAFC) for high-speed trains considering actuator faults and introduced an auxiliary system to handle input saturation. Ref. [26] designed a distributed adaptive fault-tolerant control scheme for nonlinear multi-agent systems affected by actuator faults. Ref. [27] proposed a distributed fault-tolerant control (FTC) scheme for nonlinear fractional-order (FO) multi-agent systems (MASs). Ref. [28] designed a distributed adaptive fault-tolerant controller based on the states of finite-time observers. In practical tasks, due to the large-scale movement of platforms, signal occlusion, or channel fading, communication links between unmanned platforms may be interrupted and reconnected, forming a time-varying communication topology. A robust controller is required for the changes in the topology structure.

While the aforementioned studies have made significant progress, many distributed control techniques struggle with the simultaneous occurrence of these issues. One instance of this is traditional sliding mode control (SMC), which offers robustness but often relies on periodic, high-frequency communication and is unfeasible for USV-AUV systems. Conversely, standard event-triggered methods reduce communication but may lack robustness against the significant uncertainties introduced by actuator faults. The proposed DETM + adaptive FTC method differs from these approaches by creating a synergistic loop: the DETM dynamically adjusts communication based on the control error (which is influenced by faults), while the adaptive FTC actively compensates for these faults, thereby reducing the error and, in turn, further easing the communication burden. This integrated approach provides a more efficient and resilient solution tailored for this specific heterogeneous environment. This highlights a critical research gap: the lack of a unified control framework that concurrently addresses system heterogeneity (USV-AUV), severe communication constraints (delays and DETM), and critical reliability issues (adaptive fault tolerance) within a single, stable design. While refs. [1–11] establish the importance and challenges of USV-AUV cooperation, and refs. [11–28] explore individual aspects like FTC or ETC, this paper aims to develop a cohesive solution for this specific, complex intersection.

Existing studies have separately explored issues such as heterogeneous system control, event triggering, fault-tolerant control, and communication delays; there are few results that comprehensively address these challenges within a unified framework, especially for USV-AUV cross-domain cooperative scenarios. This paper aims to solve the aforementioned challenges and propose a distributed adaptive fault-tolerant formation control scheme for heterogeneous USV-AUV systems. This paper constructs an integrated control framework capable of addressing heterogeneity, communication constraints, actuator faults, and delays simultaneously. Specifically, the method proposed in this paper includes the following key components:

1. Euler–Lagrange Modeling: This paper establishes a unified model capable of describing the dynamics of both USVs and AUVs. By parameterizing the unknown terms in the system, this paper lays down a foundation for the subsequent design of a general adaptive controller.
2. DETM: To address the problem of limited underwater acoustic communication resources, this paper includes the design of a DETM for each agent. The triggering threshold of this mechanism is correlated with the dynamic formation error of the system, which can increase the communication frequency to ensure fast convergence when the error is large, and reduce communication to save energy when the system is stable, thereby achieving an intelligent trade-off between communication efficiency and control performance.

3. Adaptive Fault-Tolerant Strategy: The controller incorporates adaptive laws, enabling it to provide an online estimate and compensate for unknown system parameters, external disturbances, and actuator faults caused by loss of effectiveness and bias. This ensures that the formation system can maintain stable performance in the face of internal faults and external uncertainties. Meanwhile, to handle time-varying communication delays, this paper incorporates delay terms into the stability analysis by constructing an appropriate Lyapunov–Krasovskii functional, ensuring the stability of the closed-loop system in the presence of delays.

The remainder of this paper is organized as follows: Section 2 introduces system modeling and problem description. Section 3 details the design of the controller incorporating DETM and the adaptive fault-tolerant strategy, and presents the stability proof. Section 4 describes the scenario settings and result analysis of the simulation experiments. Section 5 summarizes the entire paper.

2. System Modeling and Problem Description

2.1. Graph Theory and Communication Topology

This paper adopts algebraic graph theory to describe the dynamic information interaction network within the heterogeneous USV-AUV system. Due to platform movement, signal occlusion, or underwater acoustic channel fading, communication links may be interrupted and reconnected; thus, the network topology is modeled as a time-varying weighted directed graph. The set of nodes in the graph is denoted by $\mathcal{V} = \{0, 1, 2, \ldots, N\}$, where node 0 represents a leader (typically a USV) and nodes $\{1, 2, \ldots, N\}$ represent followers (which can be either USVs or AUVs). The set of directed edges is denoted by $\mathcal{E}(t) \subseteq \mathcal{V} \times \mathcal{V}$, where an edge $(j, i) \in \mathcal{E}(t)$ indicates that platform i can receive information from platform j at time t.

The topological structure associated with the graph can be described using the following matrices:

1. Adjacency Matrix: The communication links between followers are characterized by a weighted adjacency matrix $\mathbf{A}(t) = [a_{ij}(t)]_{N\times N}$. The weight $a_{ij}(t) > 0$ if and only if $(j, i) \in \mathcal{E}(t)$ and $i \neq j$; otherwise, $a_{ij}(t) = 0$. This paper follows the convention that $a_{ii}(t) = 0$ for all i.
2. Navigation Matrix: The communication links from the leader to followers are described by a diagonal navigation matrix $\mathbf{B}(t) = \text{diag}\{b_1(t), b_2(t), \ldots, b_N(t)\}$. If follower i can directly receive information from the leader, then $b_i(t) > 0$; otherwise, $b_i(t) = 0$.
3. Degree Matrix: The in-degree matrix of the follower network is a diagonal matrix $\mathbf{D}(t) = [d_{ii}(t)]_{N\times N}$, where each diagonal element is defined as follows:

$$d_{ii}(t) = \sum_{j=1}^{N} a_{ij}(t). \tag{1}$$

   This element represents the total weight of information flows received by follower i from all other followers.
4. Laplacian Matrix: The graph Laplacian matrix of the follower network is defined as follows:

$$\mathbf{L}(t) = \mathbf{D}(t) - \mathbf{A}(t). \tag{2}$$

To uniformly describe all communication relationships in controller design and stability analysis, this paper defines a composite matrix:

$$\mathbf{C}(t) = \mathbf{L}(t) + \mathbf{B}(t), \tag{3}$$

where $\mathbf{L}(t)$ captures the communication topology between followers, and $\mathbf{B}(t)$ captures the communication links from the leader to followers.

Owing to the dynamics of the communication environment, the network topology is time-varying. This paper assumes there exists a finite set of candidate topologies $\{\mathcal{G}_1, \mathcal{G}_2, \ldots, \mathcal{G}_M\}$. The active topology at time t is determined by a piecewise constant switching signal $\sigma(t) \in \{1, 2, \ldots, M\}$. This implies that there exists a time sequence $0 = t_0 < t_1 < t_2 < \cdots < \infty$ such that the communication topology remains fixed within any time interval $[t_k, t_{k+1})$. This paper assumes that the switching is not infinitely fast, i.e., it satisfies the minimum dwell time condition: $t_{k+1} - t_k \geq \tau_d$ for all k, where $\tau_d > 0$ is a positive constant.

To ensure that the leader's information can be transmitted to every follower (thereby enabling coordinated movement of the entire formation), this paper introduces the following basic assumption regarding network connectivity:

Assumption 1. *For any active topology at arbitrary time t, the composite matrix $\mathbf{C}(t)$ is nonsingular. This is equivalent to the graph containing a directed spanning tree with the leader node 0 as its root, meaning there exists a directed path from the leader node to any follower node.*

Assumption 1 is a standard and necessary condition for distributed formation control. Physically, if a follower is completely disconnected from the influence of the leader, it is impossible for it to follow the trajectory of the leader, making the formation control objective unattainable.

To aid readability, key symbols and variables used throughout the paper are summarized in Table 1.

Table 1. Summary of Key Notation.

Symbol	Definition
$\mathcal{V} = \{0, \ldots, N\}$	Set of all platforms (0 = leader, 1 … N = followers)
$\mathcal{E}(t)$	Set of directed communication edges at time t
$A(t), B(t), L(t)$	Adjacency, Navigation, and Laplacian matrices
$C(t)$	Composite matrix $L(t) + B(t)$
η_i, v_i	Position/attitude vector and linear/angular velocity vector (of agent i)
$M_i, C_i(v_i), D_i(v_i)$	Inertia, Coriolis, and Damping matrices
τ_i, τ_i^{act}	Commanded and Actual (post-fault) control input
$\Lambda_i(t), b_i(t)$	Actuator effectiveness matrix and bias fault vector
$\hat{\Lambda}_i(t), \hat{W}_i(t)$	Estimated effectiveness factor matrix and estimated RBFNN weights
$\tau_{ji}(t)$	Communication delay from platform j to i
$e_{\eta,i}, e_{v,i}$	Position and velocity formation tracking errors
$e^s_{\eta,i}, e^s_{v,i}$	Sampled state measurement error (due to DETM)
$\sigma_i(t)$	Dynamic event-triggering threshold
$s_i(t)$	Sliding mode surface variable
$W_i^*, \Phi_i(Z_i)$	Ideal and basis function vector of RBFNN

2.2. Heterogeneous Dynamic Models

To design a unified control framework adaptable to both USVs and AUVs, this paper models the dynamics of each unmanned platform using the Euler–Lagrange method. This approach provides a structured and generalized form for describing the motion of rigid bodies in fluids.

As shown in Figure 1, the operational scenario and coordinate systems are illustrated. The global inertial frame (Earth-fixed) is denoted by $O_E - X_E Y_E Z_E$. Each platform i (USV or AUV) has its own body-fixed frame, denoted as $O_{ia} - X_{ia} Y_{ia} Z_{ia}$. The Navigation USV acts as the leader (node $i = 0$), providing the reference trajectory. Follower USVs and Follower AUVs (nodes $i = 1 \ \ldots \ N$) track this leader while maintaining a desired formation. The arrows labeled Information flow depict the communication topology, indicating possible data transmission paths between the leader and followers, and among the followers themselves. Critically, communication between USVs (surface-to-surface) is high-speed (radio), while communication involving AUVs (surface-to-underwater or underwater-to-underwater) relies on low-speed, high-delay acoustic links, posing a significant control challenge.

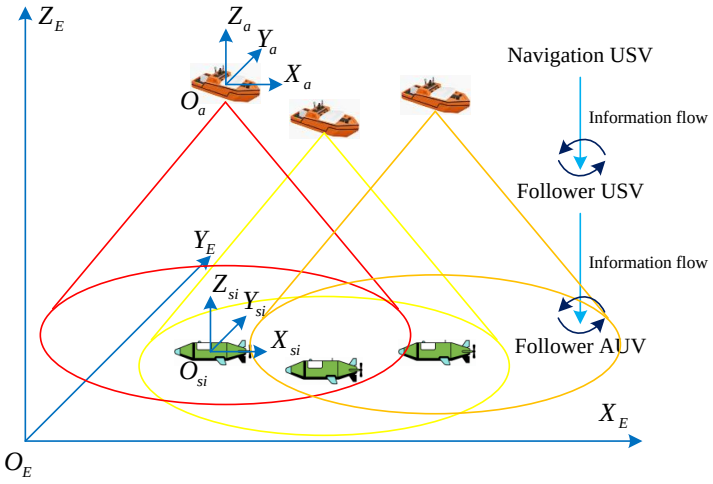

Figure 1. USV-AUV Heterogeneous System.

For the i-th unmanned platform in the system, its motion in six degrees of freedom (DOF) can be described by coupled dynamic and kinematic equations. As shown in Figure 1, the kinematic equation characterizes the velocity transformation from the platform's body-fixed frame to the inertial frame:

$$\dot{\boldsymbol{\eta}}_i = \mathbf{J}(\boldsymbol{\eta}_i)\boldsymbol{\nu}_i, \tag{4}$$

where $\boldsymbol{\eta}_i = [x_i, y_i, z_i, \phi_i, \theta_i, \psi_i]^T$ denotes the position and attitude (Euler angles: roll ϕ_i, pitch θ_i, yaw ψ_i) vector of the platform in the inertial frame; $\boldsymbol{\nu}_i = [u_i, v_i, w_i, p_i, q_i, r_i]^T$ represents the linear and angular velocity vector in the body-fixed frame; and $\mathbf{J}(\boldsymbol{\eta}_i) \in \mathbb{R}^{6\times6}$ is the coordinate transformation matrix from the body-fixed frame to the inertial frame.

The dynamic equation, derived from Newton–Euler equations, describes the relationship between the applied forces/moments and the platform's acceleration:

$$\mathbf{M}_i\dot{\boldsymbol{\nu}}_i + \mathbf{C}_i(\boldsymbol{\nu}_i)\boldsymbol{\nu}_i + \mathbf{D}_i(\boldsymbol{\nu}_i)\boldsymbol{\nu}_i + \mathbf{g}_i(\boldsymbol{\eta}_i) = \boldsymbol{\tau}_i + \boldsymbol{\delta}_i, \tag{5}$$

where $\mathbf{M}_i \in \mathbb{R}^{6\times6}$ is a symmetric positive-definite inertia matrix, which includes the rigid-body mass and added mass of the fluid. $\mathbf{C}_i(\boldsymbol{\nu}_i) \in \mathbb{R}^{6\times6}$ is the Coriolis and centripetal matrix. $\mathbf{D}_i(\boldsymbol{\nu}_i) \in \mathbb{R}^{6\times6}$ is the hydrodynamic damping matrix, typically containing linear and nonlinear terms. $\mathbf{g}_i(\boldsymbol{\eta}_i) \in \mathbb{R}^6$ is the restoring force and moment vector generated by gravity and buoyancy. $\boldsymbol{\tau}_i \in \mathbb{R}^6$ is the control input vector (forces/moments) generated by actuators such as propellers and rudders. $\boldsymbol{\delta}_i \in \mathbb{R}^6$ represents the combined effect of unmodeled dynamics and external environmental disturbances (e.g., wind, waves, currents).

Manifestation of Heterogeneity: Although Equations (3) and (4) have a unified form, the dynamic characteristics of USVs and AUVs exhibit significant differences within this model—this is precisely where the system's heterogeneity lies:

1. Dimension Reduction: USVs primarily move in the horizontal plane, so their model can usually be simplified to 3 DOF (surge u_i, sway v_i, yaw r_i), i.e., $\boldsymbol{\eta}_i = [x_i, y_i, \psi_i]^T$ and $\boldsymbol{\nu}_i = [u_i, v_i, r_i]^T$. Their roll, pitch, and heave motions are generally treated as bounded disturbances.
2. Restoring Force/Moment: For AUVs, the restoring force/moment term $\mathbf{g}_i(\boldsymbol{\eta}_i)$ is crucial. It is determined by the positions of the center of gravity and center of buoyancy, and is key to maintaining attitude stability. For USVs, this term can usually be neglected in the horizontal-plane model.
3. Inertia and Damping: AUVs are fully submerged in water, so their added mass effect and hydrodynamic damping are far more significant and complex than those of USVs floating on the water surface.
4. External Disturbances: USVs are mainly affected by wind and waves, while AUVs are primarily influenced by ocean currents. The characteristics and models of these disturbances are completely different.

To facilitate the subsequent design of a unified controller, this paper converts the above Euler–Lagrange model into a state-space form. Define the system state as $\boldsymbol{\eta}_i$ and $\boldsymbol{\nu}_i$. Taking the derivative of $\boldsymbol{\eta}_i$ gives the following:

$$\ddot{\boldsymbol{\eta}}_i = \dot{\mathbf{J}}(\boldsymbol{\eta}_i)\boldsymbol{\nu}_i + \mathbf{J}(\boldsymbol{\eta}_i)\dot{\boldsymbol{\nu}}_i$$

Solving for $\dot{\boldsymbol{\nu}}_i$ from Equation (4) and substituting it into the above equation, while noting that $\mathbf{J}^{-1}(\boldsymbol{\eta}_i)$ exists, this paper obtains the following second-order nonlinear system model:

$$\ddot{\boldsymbol{\eta}}_i = \mathbf{f}_i(\boldsymbol{\eta}_i, \boldsymbol{\nu}_i) + \mathbf{G}_i(\boldsymbol{\eta}_i)\boldsymbol{\tau}_i + \mathbf{d}_i, \tag{6}$$

where $\mathbf{f}_i(\boldsymbol{\eta}_i, \boldsymbol{\nu}_i) = \mathbf{J}(\boldsymbol{\eta}_i)\mathbf{M}_i^{-1}[-\mathbf{C}_i(\boldsymbol{\nu}_i)\boldsymbol{\nu}_i - \mathbf{D}_i(\boldsymbol{\nu}_i)\boldsymbol{\nu}_i - \mathbf{g}_i(\boldsymbol{\eta}_i)] + \dot{\mathbf{J}}(\boldsymbol{\eta}_i)\boldsymbol{\nu}_i$ represents the internal nonlinear dynamics of the system; $\mathbf{G}_i(\boldsymbol{\eta}_i) = \mathbf{J}(\boldsymbol{\eta}_i)\mathbf{M}_i^{-1}$ is the control input gain matrix; and $\mathbf{d}_i = \mathbf{J}(\boldsymbol{\eta}_i)\mathbf{M}_i^{-1}\boldsymbol{\delta}_i$ is the lumped unknown disturbance term.

Remark 1. *Equation (5) provides a unified mathematical model for the entire heterogeneous system. Although the form is identical, the specific forms and parameter values of the function* $\mathbf{f}_i$ *and matrix* $\mathbf{G}_i$ *for each platform i are different—this accurately characterizes the dynamic heterogeneity between USVs and AUVs.*

Remark 2. *In practical applications, matrices such as the inertia matrix* $\mathbf{M}_i$ *and damping matrix* $\mathbf{D}_i$ *usually contain parameters that are difficult to obtain accurately. Therefore, in subsequent sections, this paper assumes that the function* $\mathbf{f}_i$ *and matrix* $\mathbf{G}_i$ *include unknown but bounded parameters. This provides a theoretical basis for using adaptive control methods to online estimate and compensate for these uncertainties.*

2.3. Actuator Faults and Communication Delays

While Equation (6) and Remark 2 establish the unified ideal dynamic model and its inherent uncertainties, a robust control design for real-world marine operations must also account for non-ideal hardware and communication failures. Therefore, the following sections explicitly model two of the most critical challenges: actuator faults and communication delays.

In practical marine operating environments, the physical components and communication links of unmanned platforms cannot work ideally. To make the control strategy more applicable to real-world scenarios, this section mathematically models two key non-ideal factors: actuator faults and communication delays.

(1) Actuator Fault Model

For the k-th actuator of the i-th unmanned platform, the relationship between its actual output and the command issued by the controller is modeled as follows:

$$\tau_{i,k}^{\text{act}} = \lambda_{i,k}(t)\tau_{i,k} + b_{i,k}(t), \tag{7}$$

where $\lambda_{i,k}(t) \in (0,1]$ is the unknown time-varying effectiveness factor: $\lambda_{i,k}(t) = 1$ indicates the actuator works normally; $\lambda_{i,k}(t) < 1$ means the actuator is partially failed and can only output a fraction of the command; $\lambda_{i,k}(t) = 0$ represents complete actuator failure (not considered in this paper due to Assumption 2). $b_{i,k}(t)$ is the unknown time-varying additive bias fault, such as an actuator jamming at a non-zero position.

Integrating the faults of all actuators into a vector form, the actual control input of the i-th platform is as follows:

$$\boldsymbol{\tau}_i^{\text{act}} = \boldsymbol{\Lambda}_i(t)\boldsymbol{\tau}_i + \boldsymbol{b}_i(t), \tag{8}$$

where $\boldsymbol{\Lambda}_i(t) = \text{diag}\{\lambda_{i,1}(t), \lambda_{i,2}(t), \ldots, \lambda_{i,6}(t)\}$ is the diagonal matrix of effectiveness factors, and $\boldsymbol{b}_i(t) = [b_{i,1}(t), b_{i,2}(t), \ldots, b_{i,6}(t)]^T$ is the bias fault vector.

Substituting this fault model (7) into the system dynamic Equation (5), the system model in the presence of actuator faults is obtained as follows:

$$\ddot{\boldsymbol{\eta}}_i = \mathbf{f}_i(\boldsymbol{\eta}_i, \boldsymbol{\nu}_i) + \mathbf{G}_i(\boldsymbol{\eta}_i)\boldsymbol{\Lambda}_i(t)\boldsymbol{\tau}_i + \mathbf{G}_i(\boldsymbol{\eta}_i)\boldsymbol{b}_i(t) + \mathbf{d}_i. \tag{9}$$

For controller design and stability analysis, this paper makes the following reasonable assumption:

Assumption 2. *Actuator faults are unknown but bounded. Specifically, there exist unknown positive constants $\underline{\lambda}_i$ and $\overline{b}_i$ such that for all $t \geq 0$, $\lambda_{i,k}(t) \geq \underline{\lambda}_i > 0$ (for $k = 1, 2, \ldots, 6$) and $\|\boldsymbol{b}_i(t)\| \leq \overline{b}_i$ hold. This assumption implies that the actuator will not experience complete failure or control direction reversal, and the fault bias will not grow unbounded.*

This assumption is physically reasonable. The condition $\underline{\lambda}_i > 0$ implies actuators do not reverse direction or fail completely (which would require replacement, not control compensation). Bounded bias $||b_i(t)|| \leq \overline{b}_i$ reflects physical limitations, such as a rudder being stuck at a maximum angle or a thruster failing to a fixed (but not infinite) RPM.

(2) Communication Delay Model

Cross-domain collaboration between USVs and AUVs relies heavily on communication. Communication between USVs typically uses high-rate, low-latency radio, while communication between USVs and AUVs must rely on low-rate, high-latency underwater acoustic communication. This heterogeneous, time-varying communication delay is a key factor that must be considered in system design.

This paper assumes that there exists a time-varying, bounded communication delay $\tau_{ji}(t) > 0$ in the information transmission from platform j to platform i. Therefore, the state information received by platform i at time t from platform j is actually the state of platform j at time $t - \tau_{ji}(t)$, i.e., $\boldsymbol{\eta}_j(t - \tau_{ji}(t))$ and $\boldsymbol{\nu}_j(t - \tau_{ji}(t))$.

To ensure that the stability of the system can be theoretically analyzed, this paper makes the following standard assumption about communication delays:

Assumption 3. *Communication delays and their time derivatives are bounded. That is, there exist known positive constants τ_{max} and $\dot{\tau}_{max}$ such that for all $i, j \in \mathcal{V}$ and $t \geq 0$, the following holds:*

$$0 < \tau_{ji}(t) \leq \tau_{max}, \tag{10}$$

$$\dot{\tau}_{ji}(t) \leq \dot{\tau}_{max} < 1. \tag{11}$$

Equation (9) ensures that the delay will not be infinite, while Equation (10) limits the rate of change of the delay to avoid excessively fast variations. This is a key prerequisite for analyzing the stability of time-delay systems using Lyapunov–Krasovskii functionals.

The upper bound τ_{max} is physically guaranteed, as communication (even acoustic) does not take infinite time. The bound $\dot{\tau}_{max} < 1$ assumes the rate of change of the delay (e.g., due to relative motion changing the acoustic path length) is not faster than time itself, which is a mild and standard assumption for stability analysis of time-delay systems.

Remark 3. *Combining the above models, the subsequent controller design faces a critical challenge: each agent must calculate the control command based on its own current state $\boldsymbol{\eta}_i(t), \boldsymbol{\nu}_i(t)$, as well as the outdated information from neighbors that is both event-triggered and delayed. This command needs to actively compensate for the negative impacts caused by unknown effectiveness factors and bias faults, thereby achieving cooperative control of the entire heterogeneous formation.*

2.4. Formation Control Problem Modeling

Based on the aforementioned system dynamics, actuator fault, and communication delay models, this section presents an accurate mathematical modeling of the cooperative formation control problem for the heterogeneous USV-AUV system.

The core objective of formation control is to drive a group of follower unmanned platforms to accurately track the motion of a leader, while maintaining a predefined and potentially time-varying geometric configuration among them.

For each follower i $(i = 1, 2, \ldots, N)$, this paper defines a desired formation vector $\boldsymbol{\delta}_i(t) \in \mathbb{R}^n$ (where $n = 3$ for USVs and $n = 6$ for AUVs, corresponding to their respective degrees of freedom). This vector describes the desired position and attitude of follower i relative to the leader. Thus, the desired state trajectory of follower i is defined as follows:

$$\boldsymbol{\eta}_{i,d}(t) = \boldsymbol{\eta}_0(t) + \boldsymbol{\delta}_i(t), \tag{12}$$

where $\boldsymbol{\eta}_0(t) \in \mathbb{R}^n$ denotes the state vector (position and attitude) of the leader. This paper assumes that the leader's state and its first and second time derivatives $(\boldsymbol{\eta}_0(t), \dot{\boldsymbol{\eta}}_0(t), \ddot{\boldsymbol{\eta}}_0(t))$ are accessible to followers that can communicate directly with the leader, and all these signals are bounded.

This paper defines the formation tracking error of follower i as the difference between its actual state and the desired state:

$$\boldsymbol{e}_{\eta,i}(t) = \boldsymbol{\eta}_i(t) - \boldsymbol{\eta}_{i,d}(t). \tag{13}$$

The entire formation control task can be formally stated as follows: design a control law such that the formation tracking error of all followers converges to and remains within a small neighborhood.

Definition 1. *Consider an unmanned system consisting of one leader and N followers (USVs/AUVs), where:*

1. *The dynamics of each follower are described by the nonlinear Equation (5);*
2. *The actuators of each follower may suffer from unknown effectiveness loss and bias faults as shown in (8), with fault parameters satisfying Assumption 2;*
3. *Information interaction within the system is conducted through a time-varying communication topology that satisfies Assumption 1;*
4. *Information transmission between any two unmanned platforms involves time-varying bounded delays as described in (9) and (10), which satisfy Assumption 3.*

The core task of this paper is to design a distributed adaptive fault-tolerant control protocol for each follower. Under the combined conditions of heterogeneity, faults, delays, event triggering, and time-varying topology, this protocol aims to ensure that for any given bounded initial conditions, all signals in the closed-loop system (including states, control inputs, and adaptive parameter estimates) are bounded, and the formation tracking error of all followers asymptotically converges to an adjustable compact set that can be arbitrarily tuned by design parameters. Specifically, there exists a small positive constant $\epsilon > 0$ such that

$$\lim_{t\to\infty} \|e_{\eta,i}(t)\| \leq \epsilon \quad \forall\, i = 1, 2, \ldots, N. \tag{14}$$

3. Formation Control Method Design and Stability Analysis

This section designs a distributed adaptive fault-tolerant controller to solve the formation control problem defined in Definition 1 of Section 2.4. The core of this method lies in integrating a dynamic event-triggered mechanism to achieve efficient communication, and combining adaptive technology to handle system uncertainties, actuator faults, and communication delays. The control architecture is shown in Figure 2.

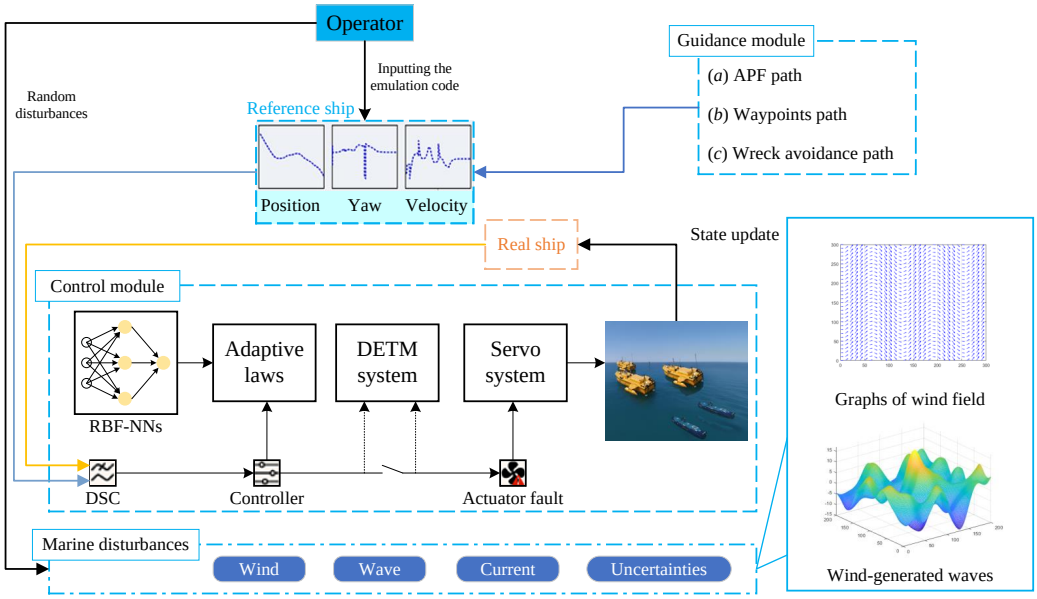

Figure 2. The flowchart of the closed–loop system.

3.1. Dynamic Event-Triggered Mechanism

To enable the communication strategy to adapt to the dynamic performance of the system, this paper designs a DETM. Its core idea is that the necessity of communication is determined by a dynamic threshold related to the system state, thereby minimizing the network communication load while ensuring the accuracy of formation control.

For each follower i $(i = 1, 2, \ldots, N)$, its communication moments are determined by an event-triggering time sequence $\{t_{i,k}\}_{k=0}^{\infty}$ where $t_{i,0} = 0 < t_{i,1} < t_{i,2} < \cdots < \infty$. At each triggering moment $t_{i,k}$, platform i samples its own state and broadcasts it to all its neighboring platforms through the network. Between two consecutive triggering moments, i.e., for $t \in [t_{i,k}, t_{i,k+1})$, both the controller of platform i and the controllers of its neighboring nodes calculate using the sampled values fixed by a "zero-order holder". This intermittent sampling introduces a measurement error between the sampled state and the real-time state, which is defined as follows:

$$e^s_{\eta,i}(t) = \eta_i(t_{i,k}) - \eta_i(t), \quad e^s_{v,i}(t) = v_i(t_{i,k}) - v_i(t) \quad \forall t \in [t_{i,k}, t_{i,k+1}), \tag{15}$$

where $\boldsymbol{e}^s_{\eta,i}(t)$ and $\boldsymbol{e}^s_{v,i}(t)$ correspond to the measurement errors of position/attitude and velocity, respectively. Obviously, $\boldsymbol{e}^s_{\eta,i}(t_{i,k}) = \mathbf{0}$ and $\boldsymbol{e}^s_{v,i}(t_{i,k}) = \mathbf{0}$ at the triggering instant.

The next triggering moment $t_{i,k+1}$ is determined by the following rule:

$$t_{i,k+1} = \inf\Big\{ t > t_{i,k} \mid \|\boldsymbol{\xi}_i(t)\|^2 \geq \sigma_i(t) \Big\}, \tag{16}$$

where inf denotes the infimum. Within a set of time points, the infimum represents the smallest time point in the set, and its function is to capture the first instant that satisfies the triggering condition. It can be seen from rule (15) that an event is triggered when the norm of the measurement error $\boldsymbol{\xi}_i(t) = \left[(\boldsymbol{e}^s_{\eta,i}(t))^T, (\boldsymbol{e}^s_{v,i}(t))^T \right]^T$ increases beyond a dynamically changing threshold $\sigma_i(t)$.

Different from the static event-triggered mechanism, the threshold here is not a fixed positive constant but an internal dynamic variable. Its update law is designed as follows:

$$\dot{\sigma}_i(t) = -\alpha_i \sigma_i(t) - \beta_i \|\boldsymbol{s}_i(t)\|^2 + \gamma_i, \tag{17}$$

where $\alpha_i > 0$, $\beta_i > 0$, and $\gamma_i > 0$ are all positive design parameters, and $\boldsymbol{s}_i(t)$ is the sliding mode surface variable to be defined in the next section, which directly reflects the control error of the system.

Remark 4. *The design of this dynamic threshold update law (16) has clear physical meanings:*

1. *When the system control error is large, the term $-\beta_i \|\boldsymbol{s}_i(t)\|^2$ dominates, making $\dot{\sigma}_i(t)$ a relatively large negative number, and the threshold $\sigma_i(t)$ decreases rapidly. A smaller threshold means a lower tolerance for measurement errors, which will lead to more frequent event triggering, thereby providing the controller with more timely state information to suppress errors.*
2. *When the system tends to be stable and the control error becomes very small, $\|\boldsymbol{s}_i(t)\|^2 \approx 0$, which will make $\dot{\sigma}_i(t) \approx -\alpha_i \sigma_i(t) + \gamma_i$. At this point, $\sigma_i(t)$ will gradually stabilize around γ_i/α_i. The threshold is relatively large at this time, allowing the measurement error to vary within a larger range, thus greatly reducing the communication frequency in the stable state and saving energy consumption.*
3. *The existence of the constant term γ_i ensures that the threshold has a positive lower bound even in the ideal case where the error is zero, which is crucial for avoiding the Zeno phenomenon.*

The designed DETM can effectively avoid the Zeno phenomenon, i.e., the occurrence of an infinite number of triggers within a finite time. This is because after any triggering moment $t_{i,k}$, the measurement error starts to increase from zero ($\boldsymbol{\xi}_i(t_{i,k}) = \mathbf{0}$). Since the system dynamics (i.e., $\dot{\boldsymbol{\eta}}_i(t), \dot{\boldsymbol{v}}_i(t)$) are bounded on any compact set, the growth rate of the measurement error is also bounded. Meanwhile, it can be seen from (16) that the dynamic threshold $\sigma_i(t)$ remains positive at all times. Therefore, the measurement error needs a non-zero period of time to grow from 0 to the positive threshold. Hence, there exists a positive lower bound for the minimum time interval between two consecutive triggers, thereby eliminating the Zeno phenomenon.

3.2. Distributed Adaptive Fault-Tolerant Controller

The objective of this section is to design a distributed control input for each follower i. This paper adopts a strategy that combines Sliding Mode Control (SMC) with adaptive control: SMC provides robustness against uncertainties and disturbances, while adaptive technology is used to online estimate and compensate for unknown system and fault parameters.

3.2.1. Composite Error and Sliding Mode Surface Design

To achieve the formation objective, this paper first needs to define an error variable that comprehensively reflects the position and velocity tracking performance. For this purpose, this paper designs a sliding mode surface for each follower i:

$$\boldsymbol{s}_i(t) = \boldsymbol{e}_{v,i}(t) + \boldsymbol{K}_i \boldsymbol{e}_{\eta,i}(t), \tag{18}$$

where $\boldsymbol{e}_{\eta,i}(t) = \boldsymbol{\eta}_i(t) - \boldsymbol{\eta}_{i,d}(t)$ and $\boldsymbol{e}_{v,i}(t) = \dot{\boldsymbol{\eta}}_i(t) - \dot{\boldsymbol{\eta}}_{i,d}(t)$ are the position and velocity formation tracking errors respectively, and $\boldsymbol{K}_i \in \mathbb{R}^{n\times n}$ (with $n = 3$ for USVs and $n = 6$ for AUVs) is a symmetric positive-definite design parameter matrix. The core of the control task is to design a control law such that the sliding mode variable $\boldsymbol{s}_i(t)$ can quickly converge to zero and remain within its neighborhood; according to sliding mode theory, this ensures that the formation errors $\boldsymbol{e}_{\eta,i}(t)$ and $\boldsymbol{e}_{v,i}(t)$ also converge to the vicinity of zero.

Taking the time derivative of the sliding mode surface (17), we obtain the following:

$$\dot{\boldsymbol{s}}_i(t) = \ddot{\boldsymbol{\eta}}_i(t) - \ddot{\boldsymbol{\eta}}_{i,d}(t) + \boldsymbol{K}_i \dot{\boldsymbol{e}}_{\eta,i}(t) = \ddot{\boldsymbol{\eta}}_i(t) - \ddot{\boldsymbol{\eta}}_{i,d}(t) + \boldsymbol{K}_i \boldsymbol{e}_{v,i}(t). \tag{19}$$

Substituting the system dynamic Equation (8) with faults into the above expression, we have the following:

$$\begin{aligned} \dot{\boldsymbol{s}}_i(t) = {} & \mathbf{f}_i(\boldsymbol{\eta}_i, \boldsymbol{\nu}_i) + \mathbf{G}_i(\boldsymbol{\eta}_i)\boldsymbol{\Lambda}_i(t)\boldsymbol{\tau}_i(t) + \mathbf{G}_i(\boldsymbol{\eta}_i)\boldsymbol{b}_i(t) + \mathbf{d}_i(t) \\ & - \ddot{\boldsymbol{\eta}}_{i,d}(t) + \boldsymbol{K}_i \boldsymbol{e}_{v,i}(t). \end{aligned} \tag{20}$$

The right-hand side of the above equation contains numerous unknown terms: the nonlinear function $\mathbf{f}_i(\boldsymbol{\eta}_i, \boldsymbol{\nu}_i)$, input gain $\mathbf{G}_i(\boldsymbol{\eta}_i)$, fault parameters $\boldsymbol{\Lambda}_i(t)$ and $\boldsymbol{b}_i(t)$, as well as external disturbances $\mathbf{d}_i(t)$.

3.2.2. Uncertainty Handling and Function Approximation

To address these complex uncertainties, this paper integrates all unknown terms. Rewrite Equation (19) as follows:

$$\dot{\boldsymbol{s}}_i(t) = \mathbf{G}_i(\boldsymbol{\eta}_i)\boldsymbol{\Lambda}_i(t)\boldsymbol{\tau}_i(t) + \mathbf{f}_{i,\text{total}}(\boldsymbol{Z}_i(t)), \tag{21}$$

where $\mathbf{f}_{i,\text{total}}(\boldsymbol{Z}_i(t)) = \mathbf{f}_i(\boldsymbol{\eta}_i, \boldsymbol{\nu}_i) + \mathbf{G}_i(\boldsymbol{\eta}_i)\boldsymbol{b}_i(t) + \mathbf{d}_i(t) - \ddot{\boldsymbol{\eta}}_{i,d}(t) + \boldsymbol{K}_i \boldsymbol{e}_{v,i}(t)$, and $\boldsymbol{Z}_i(t)$ is a comprehensive state vector that includes all variables required for calculating $\mathbf{f}_{i,\text{total}}$.

This paper integrates all unknown terms that do not contain the control input into a single nonlinear function $\mathbf{f}_{i,\text{total}}(\boldsymbol{Z}_i(t))$, i.e.,

$$\mathbf{f}_{i,\text{total}}(\boldsymbol{Z}_i(t)) = \mathbf{W}_i^* \boldsymbol{\Phi}_i(\boldsymbol{Z}_i(t)) + \boldsymbol{\varepsilon}_i(t), \tag{22}$$

where $\boldsymbol{Z}_i(t) \in \mathbb{R}^p$ (with p being the dimension of the input vector) is a vector containing all variables needed for computation; $\mathbf{W}_i^* \in \mathbb{R}^{n\times m}$ is the ideal neural network weight matrix (with m being the number of neurons); $\boldsymbol{\Phi}_i(\boldsymbol{Z}_i(t)) = [\phi_{i1}(\boldsymbol{Z}_i(t)), \phi_{i2}(\boldsymbol{Z}_i(t)), \ldots, \phi_{im}(\boldsymbol{Z}_i(t))]^T$ is the radial basis function vector (a common choice for $\phi_{ij}(\cdot)$ is the Gaussian function: $\phi_{ij}(\boldsymbol{Z}_i) = \exp(-\|\boldsymbol{Z}_i - \boldsymbol{c}_{ij}\|^2/(2\sigma_{ij}^2))$, where $\boldsymbol{c}_{ij}$ and σ_{ij} are the center and width of the j-th radial basis function respectively); and $\boldsymbol{\varepsilon}_i(t) \in \mathbb{R}^n$ is the bounded approximation error, satisfying $\|\boldsymbol{\varepsilon}_i(t)\| \le \varepsilon_{i,\max}$ (with $\varepsilon_{i,\max} > 0$ being an unknown bounded constant).

To enable the RBFNN to fully learn and compensate for the complex dynamics and uncertainties of the system, its input vector $\boldsymbol{Z}_i(t)$ should be designed as a comprehensive state vector that includes all relevant available information. Its specific form can be expressed as follows:

$$\boldsymbol{Z}_i(t) = \left[\boldsymbol{\eta}_i^T(t), \dot{\boldsymbol{\eta}}_i^T(t), \boldsymbol{\eta}_0^T(t), \dot{\boldsymbol{\eta}}_0^T(t), \ddot{\boldsymbol{\eta}}_0^T(t), \boldsymbol{\delta}_i^T(t), \dot{\boldsymbol{\delta}}_i^T(t), \ddot{\boldsymbol{\delta}}_i^T(t), \bigcup_{j\in\mathcal{N}_i} \left\{ \boldsymbol{\eta}_j^T(t-\tau_{ji}(t)), \dot{\boldsymbol{\eta}}_j^T(t-\tau_{ji}(t)) \right\} \right]^T, \tag{23}$$

where $\boldsymbol{\eta}_i(t), \dot{\boldsymbol{\eta}}_i(t)$ are the real-time state and velocity of platform i itself. $\boldsymbol{\eta}_0(t), \dot{\boldsymbol{\eta}}_0(t), \ddot{\boldsymbol{\eta}}_0(t)$ are the available position/attitude, velocity, and acceleration of the leader. $\boldsymbol{\delta}_i(t), \dot{\boldsymbol{\delta}}_i(t), \ddot{\boldsymbol{\delta}}_i(t)$ are the preset formation vector and its first and second derivatives. $\bigcup_{j\in\mathcal{N}_i} \left\{ \boldsymbol{\eta}_j(t-\tau_{ji}(t)), \dot{\boldsymbol{\eta}}_j^T(t-\tau_{ji}(t)) \right\}$ contains the position/attitude and velocity information received from all neighboring platforms $j \in \mathcal{N}_i$ (with $\mathcal{N}_i$ denoting the neighbor set of platform i).

3.2.3. Distributed Adaptive Fault-Tolerant Control Law

Based on the above analysis, this paper can now design the control law. The goal is to select $\boldsymbol{\tau}_i(t)$ to offset unknown terms and stabilize the sliding mode dynamics. Following the certainty equivalence principle, this paper uses the estimated values of the RBFNN to replace the unknown $\mathbf{f}_{i,\text{total}}(\boldsymbol{Z}_i(t))$, and use the estimated values of fault parameters to compensate for effectiveness loss.

Thus, this paper proposes the following distributed adaptive fault-tolerant control law:

$$\boldsymbol{\tau}_i(t) = \hat{\boldsymbol{\Lambda}}_i^{-1}(t)\mathbf{G}_i^{-1}(\boldsymbol{\eta}_i(t)) \left[-\hat{\mathbf{W}}_i(t)\boldsymbol{\Phi}_i(\boldsymbol{Z}_i(t)) - \boldsymbol{K}_{s,i}\boldsymbol{s}_i(t) - \boldsymbol{K}_{r,i}\tanh\left(\frac{\boldsymbol{s}_i(t)}{\epsilon_i}\right) \right], \tag{24}$$

where $\hat{\boldsymbol{\Lambda}}_i(t) = \text{diag}\{\hat{\lambda}_{i1}(t), \hat{\lambda}_{i2}(t), \ldots, \hat{\lambda}_{in}(t)\}$ and $\hat{\mathbf{W}}_i(t) \in \mathbb{R}^{n\times m}$ are the online estimates of the unknown effectiveness factor matrix $\boldsymbol{\Lambda}_i(t)$ and RBFNN weight matrix $\mathbf{W}_i^*$. $\boldsymbol{K}_{s,i} \in \mathbb{R}^{n\times n}$ and $\boldsymbol{K}_{r,i} \in \mathbb{R}^{n\times n}$ are symmetric positive-definite sliding mode control gain matrices: $\boldsymbol{K}_{s,i}$ is used to ensure convergence, while $\boldsymbol{K}_{r,i}$ is used to robustly suppress approximation errors and disturbances. $\epsilon_i > 0$ is the boundary layer thickness; to avoid the chattering phenomenon, the traditional sign function $\text{sgn}(\boldsymbol{s}_i(t))$ is usually replaced by a smooth saturation function or hyperbolic tangent function $\tanh(\boldsymbol{s}_i(t)/\epsilon_i)$ in practical applications (satisfying $|\tanh(x)| \leq 1$ for any x). The vector $\boldsymbol{Z}_i(t)$ serves as the input to the RBFNN and is composed of the platform's own state and the event-triggered, delayed information it receives from neighbors, which ensures the distributed nature of the control law.

To update the estimated parameters online, this paper designs the following adaptive laws, the effectiveness of which will be proven in the stability analysis in the next section:

$$\dot{\hat{\boldsymbol{\Lambda}}}_i(t) = \boldsymbol{\Gamma}_{\Lambda,i}\left[\text{diag}\left(\mathbf{G}_i^{-1}(\boldsymbol{\eta}_i(t))\boldsymbol{\tau}_i(t)\boldsymbol{s}_i^T(t) \right) - \sigma_{\Lambda,i}\hat{\boldsymbol{\Lambda}}_i(t) \right], \tag{25}$$

$$\dot{\hat{\mathbf{W}}}_i(t) = \boldsymbol{\Gamma}_{W,i}\left[\boldsymbol{s}_i(t)\boldsymbol{\Phi}_i^T(\boldsymbol{Z}_i(t)) - \sigma_{W,i}\hat{\mathbf{W}}_i(t) \right], \tag{26}$$

where $\boldsymbol{\Gamma}_{\Lambda,i} \in \mathbb{R}^{n\times n}$ and $\boldsymbol{\Gamma}_{W,i} \in \mathbb{R}^{n\times m}$ are positive-definite adaptive learning rate matrices, which determine the convergence speed of the parameter estimates. $\sigma_{\Lambda,i} > 0$ and $\sigma_{W,i} > 0$ are small positive constants, which are used to enhance the robustness of the adaptive laws and prevent parameter estimate drift (the σ-modification terms $\sigma_{\Lambda,i}\hat{\boldsymbol{\Lambda}}_i(t)$ and $\sigma_{W,i}\hat{\mathbf{W}}_i(t)$ ensure that the estimates remain bounded even when the excitation of the system is insufficient).

3.3. Stability Analysis

This section aims to prove the closed-loop stability of the heterogeneous USV-AUV formation system through rigorous Lyapunov stability theory, under the combined action of the designed distributed adaptive fault-tolerant controller (22), adaptive laws (23) and (24), and dynamic event-triggered mechanism (15) and (16).

Theorem 1. *Consider the USV-AUV formation system described by Equation (8) that satisfies Assumptions 1–3. If the distributed control law (22), adaptive laws (23) and (24), and dynamic event-triggered mechanism (15) and (16) are adopted, then by selecting appropriate design parameters, all signals in the closed-loop system (including state errors, parameter estimation errors, and dynamic thresholds) can be guaranteed to be semi-globally uniformly ultimately bounded (SGUUB).*

Proof of Theorem 1. To analyze the stability of the entire system, this paper constructs a composite Lyapunov–Krasovskii functional, which consists of four parts corresponding to sliding mode dynamics, parameter estimation errors, dynamic event-triggered thresholds, and communication delays, respectively:

$$\mathcal{V}(t) = \sum_{i=1}^{N}[\mathcal{V}_{i1}(t) + \mathcal{V}_{i2}(t) + \mathcal{V}_{i3}(t) + \mathcal{V}_{i4}(t)], \tag{27}$$

where each component is defined as follows:

$$\mathcal{V}_{i1}(t) = \frac{1}{2}\boldsymbol{s}_i^T(t)\boldsymbol{s}_i(t), \tag{28}$$

$$\mathcal{V}_{i2}(t) = \frac{1}{2}\mathrm{tr}\Big(\tilde{\boldsymbol{\Lambda}}_i^T(t)\boldsymbol{\Gamma}_{\Lambda,i}^{-1}\tilde{\boldsymbol{\Lambda}}_i(t)\Big) + \frac{1}{2}\mathrm{tr}\Big(\tilde{\mathbf{W}}_i^T(t)\boldsymbol{\Gamma}_{W,i}^{-1}\tilde{\mathbf{W}}_i(t)\Big), \tag{29}$$

$$\mathcal{V}_{i3}(t) = \frac{1}{2\alpha_i}\left(\sigma_i(t) - \frac{\gamma_i}{\alpha_i}\right)^2, \tag{30}$$

$$\mathcal{V}_{i4}(t) = \sum_{j\in\mathcal{N}_i}\int_{t-\tau_{ji}(t)}^{t}\Big(\dot{\boldsymbol{\eta}}_j^T(\theta)\dot{\boldsymbol{\eta}}_j(\theta) + \boldsymbol{e}_{\eta,j}^{s^T(\theta)}\boldsymbol{e}_{\eta,j}^{s}(\theta)\Big)d\theta, \tag{31}$$

where $\tilde{\boldsymbol{\Lambda}}_i(t) = \boldsymbol{\Lambda}_i(t) - \hat{\boldsymbol{\Lambda}}_i(t)$ and $\tilde{\mathbf{W}}_i(t) = \mathbf{W}_i^* - \hat{\mathbf{W}}_i(t)$ are the parameter estimation errors of the effectiveness factor and RBFNN weight matrix. α_i, $\boldsymbol{\Gamma}_{\Lambda,i}$, and $\boldsymbol{\Gamma}_{W,i}$ are positive design parameters (consistent with those in Equations (16), (23), and (24)). $\tau_{ji}(t)$ is the communication delay from platform j to platform i (consistent with Assumption 3). $\mathrm{tr}(\cdot)$ denotes the trace of a matrix.

This paper calculates the time derivative of $\mathcal{V}(t)$: $\dot{\mathcal{V}}(t) = \sum_{i=1}^{N}\big[\dot{\mathcal{V}}_{i1}(t) + \dot{\mathcal{V}}_{i2}(t) + \dot{\mathcal{V}}_{i3}(t) + \dot{\mathcal{V}}_{i4}(t)\big]$.

Derivative of $\mathcal{V}_{i1}(t)$

Taking the derivative of Equation (26) and substituting the sliding mode dynamics (19) and RBFNN approximation (21), we obtain the following:

$$\begin{aligned}\dot{\mathcal{V}}_{i1}(t) &= \boldsymbol{s}_i^T(t)\dot{\boldsymbol{s}}_i(t)\\ &= \boldsymbol{s}_i^T(t)[\mathbf{G}_i(\boldsymbol{\eta}_i)\boldsymbol{\Lambda}_i(t)\boldsymbol{\tau}_i(t) + \mathbf{W}_i^*\boldsymbol{\Phi}_i(\boldsymbol{Z}_i(t)) + \boldsymbol{\varepsilon}_i(t)].\end{aligned} \tag{32}$$

When we substitute the control law (22) into Equation (30), we have the following:

$$\begin{aligned}\dot{\mathcal{V}}_{i1}(t) = \boldsymbol{s}_i^T(t)\Bigg[&\mathbf{G}_i(\boldsymbol{\eta}_i)\boldsymbol{\Lambda}_i(t)\hat{\boldsymbol{\Lambda}}_i^{-1}(t)\mathbf{G}_i^{-1}(\boldsymbol{\eta}_i)\Big(-\hat{\mathbf{W}}_i(t)\boldsymbol{\Phi}_i(\boldsymbol{Z}_i(t))\\ &- \boldsymbol{K}_{s,i}\boldsymbol{s}_i(t) - \boldsymbol{K}_{r,i}\tanh\left(\frac{\boldsymbol{s}_i(t)}{\epsilon_i}\right)\Big) + \mathbf{W}_i^*\boldsymbol{\Phi}_i(\boldsymbol{Z}_i(t)) + \boldsymbol{\varepsilon}_i(t)\Bigg].\end{aligned} \tag{33}$$

When using $\mathbf{W}_i^* = \hat{\mathbf{W}}_i(t) + \tilde{\mathbf{W}}_i(t)$ and simplifying the terms involving $\mathbf{G}_i(\boldsymbol{\eta}_i)$ and its inverse (which cancel out), we have the following:

$$\begin{aligned}\dot{\mathcal{V}}_{i1}(t) = &-\boldsymbol{s}_i^T(t)\boldsymbol{\Lambda}_i(t)\hat{\boldsymbol{\Lambda}}_i^{-1}(t)\boldsymbol{K}_{s,i}\boldsymbol{s}_i(t) - \boldsymbol{s}_i^T(t)\boldsymbol{\Lambda}_i(t)\hat{\boldsymbol{\Lambda}}_i^{-1}(t)\boldsymbol{K}_{r,i}\tanh\left(\frac{\boldsymbol{s}_i(t)}{\epsilon_i}\right) \\ &+ \boldsymbol{s}_i^T(t)\tilde{\mathbf{W}}_i(t)\boldsymbol{\Phi}_i(\boldsymbol{Z}_i(t)) + \boldsymbol{s}_i^T(t)\boldsymbol{\varepsilon}_i(t)\end{aligned}. \tag{34}$$

By Assumption 2, $\lambda_{i,k}(t) \geq \underline{\lambda}_i > 0$, so $\boldsymbol{\Lambda}_i(t)\hat{\boldsymbol{\Lambda}}_i^{-1}(t)$ is positive definite. Let $\underline{\lambda}_{\Lambda,i} = \min_k\{\lambda_{i,k}(t)/\hat{\lambda}_{i,k}(t)\} > 0$; then,

$$-\boldsymbol{s}_i^T(t)\boldsymbol{\Lambda}_i(t)\hat{\boldsymbol{\Lambda}}_i^{-1}(t)\boldsymbol{K}_{s,i}\boldsymbol{s}_i(t) \leq -\underline{\lambda}_{\Lambda,i}\lambda_{\min}(\boldsymbol{K}_{s,i})\|\boldsymbol{s}_i(t)\|^2, \tag{35}$$

where $\lambda_{\min}(\cdot)$ denotes the minimum eigenvalue of a matrix.

For the term involving the hyperbolic tangent function, using the property $x\tanh(x/\epsilon) \geq \|\boldsymbol{x}\|^2 - \epsilon n$ (for $\boldsymbol{x} \in \mathbb{R}^n$ and $\epsilon > 0$), we have the following:

$$-\boldsymbol{s}_i^T(t)\boldsymbol{\Lambda}_i(t)\hat{\boldsymbol{\Lambda}}_i^{-1}(t)\boldsymbol{K}_{r,i}\tanh\left(\frac{\boldsymbol{s}_i(t)}{\epsilon_i}\right) \leq -\underline{\lambda}_{\Lambda,i}\lambda_{\min}(\boldsymbol{K}_{r,i})\Big(\|\boldsymbol{s}_i(t)\|^2 - \epsilon_i n\Big). \tag{36}$$

Substituting Equations (33) and (34) into Equation (32), and applying Young's inequality to the cross terms ($\boldsymbol{s}_i^T\tilde{\mathbf{W}}_i\boldsymbol{\Phi}_i \leq \frac{1}{2}\|\boldsymbol{s}_i\|^2 + \frac{1}{2}\|\tilde{\mathbf{W}}_i\boldsymbol{\Phi}_i\|^2$ and $\boldsymbol{s}_i^T\boldsymbol{\varepsilon}_i \leq \frac{1}{2}\|\boldsymbol{s}_i\|^2 + \frac{1}{2}\varepsilon_{i,\max}^2$), this paper can simplify $\dot{\mathcal{V}}_{i1}(t)$ into a form bounded by negative quadratic terms and positive constant terms.

Derivative of $\mathcal{V}_{i2}(t)$

Taking the derivative of Equation (27) and substituting the adaptive laws (23) and (24), we obtain the following:

$$\dot{\mathcal{V}}_{i2}(t) = \mathrm{tr}\Big(\tilde{\boldsymbol{\Lambda}}_i^T(t)\boldsymbol{\Gamma}_{\Lambda,i}^{-1}\dot{\tilde{\boldsymbol{\Lambda}}}_i(t)\Big) + \mathrm{tr}\Big(\tilde{\mathbf{W}}_i^T(t)\boldsymbol{\Gamma}_{W,i}^{-1}\dot{\tilde{\mathbf{W}}}_i(t)\Big). \tag{37}$$

Since $\dot{\tilde{\boldsymbol{\Lambda}}}_i(t) = -\dot{\hat{\boldsymbol{\Lambda}}}_i(t)$ and $\dot{\tilde{\mathbf{W}}}_i(t) = -\dot{\hat{\mathbf{W}}}_i(t)$, substitute the adaptive laws (23) and (24):

$$\begin{aligned}\dot{\mathcal{V}}_{i2}(t) = &-\mathrm{tr}\Big(\tilde{\boldsymbol{\Lambda}}_i^T(t)\Big[\mathrm{diag}\Big(\mathbf{G}_i^{-1}\boldsymbol{\tau}_i\boldsymbol{s}_i^T\Big) - \sigma_{\Lambda,i}\hat{\boldsymbol{\Lambda}}_i(t)\Big]\Big) \\ &- \mathrm{tr}\Big(\tilde{\mathbf{W}}_i^T(t)\Big[\boldsymbol{s}_i\boldsymbol{\Phi}_i^T - \sigma_{W,i}\hat{\mathbf{W}}_i(t)\Big]\Big).\end{aligned} \tag{38}$$

Expanding the terms and using $\hat{\boldsymbol{\Lambda}}_i(t) = \boldsymbol{\Lambda}_i(t) - \tilde{\boldsymbol{\Lambda}}_i(t)$ and $\hat{\mathbf{W}}_i(t) = \mathbf{W}_i^* - \tilde{\mathbf{W}}_i(t)$, the cross terms (e.g., $\mathrm{tr}(\tilde{\boldsymbol{\Lambda}}_i^T\mathrm{diag}(\mathbf{G}_i^{-1}\boldsymbol{\tau}_i\boldsymbol{s}_i^T))$) cancel out with the corresponding terms in $\dot{\mathcal{V}}_{i1}(t)$. The remaining terms are as follows:

$$\dot{\mathcal{V}}_{i2}(t) = -\sigma_{\Lambda,i}\mathrm{tr}\Big(\tilde{\boldsymbol{\Lambda}}_i^T(t)\boldsymbol{\Lambda}_i(t)\Big) + \sigma_{\Lambda,i}\|\tilde{\boldsymbol{\Lambda}}_i(t)\|_F^2 - \sigma_{W,i}\mathrm{tr}\Big(\tilde{\mathbf{W}}_i^T(t)\mathbf{W}_i^*\Big) + \sigma_{W,i}\|\tilde{\mathbf{W}}_i(t)\|_F^2, \tag{39}$$

where $\|\cdot\|_F$ denotes the Frobenius norm of a matrix. By Assumption 2, $\boldsymbol{\Lambda}_i(t)$ is a positive definite, so the first and third terms are negative semi-definite, and the entire $\dot{\mathcal{V}}_{i2}(t)$ can be bounded by negative quadratic terms of $\tilde{\boldsymbol{\Lambda}}_i(t)$ and $\tilde{\mathbf{W}}_i(t)$.

Derivative of $\mathcal{V}_{i3}(t)$

Taking the derivative of Equation (28) and substituting the threshold dynamics (16), we get the following:

$$\begin{aligned}\dot{\mathcal{V}}_{i3}(t) &= \frac{1}{\alpha_i}\left(\sigma_i(t) - \frac{\gamma_i}{\alpha_i}\right)\dot{\sigma}_i(t) \\ &= \frac{1}{\alpha_i}\left(\sigma_i(t) - \frac{\gamma_i}{\alpha_i}\right)\left(-\alpha_i\sigma_i(t) - \beta_i\|\boldsymbol{s}_i(t)\|^2 + \gamma_i\right) \\ &= -\left(\sigma_i(t) - \frac{\gamma_i}{\alpha_i}\right)^2 - \frac{\beta_i}{\alpha_i}\left(\sigma_i(t) - \frac{\gamma_i}{\alpha_i}\right)\|\boldsymbol{s}_i(t)\|^2.\end{aligned} \tag{40}$$

The first term in Equation (38) is always non-positive. Applying Young's inequality to the second term ($-ab \leq \frac{a^2}{2} + \frac{b^2}{2}$), this paper can bound it by a negative quadratic term of $\|\boldsymbol{s}_i(t)\|$ and a positive term of $\sigma_i(t)$ (which is further bounded by the first term).

Derivative of $\mathcal{V}_{i4}(t)$

Taking the derivative of Equation (29) and using Leibniz's rule for integration, we obtain the following:

$$\begin{aligned}\dot{\mathcal{V}}_{i4}(t) = \sum_{j\in\mathcal{N}_i}[&\dot{\boldsymbol{\eta}}_j^T(t)\dot{\boldsymbol{\eta}}_j(t) + \boldsymbol{e}_{\eta,j}^{s^T(t)}\boldsymbol{e}_{\eta,j}^s(t) - (1-\dot{\tau}_{ji}(t))(\dot{\boldsymbol{\eta}}_j^T(t-\tau_{ji}(t))\dot{\boldsymbol{\eta}}_j(t-\tau_{ji}(t)) \\ &+ \boldsymbol{e}_{\eta,j}^{s^T(t-\tau_{ji}(t))}\boldsymbol{e}_{\eta,j}^s(t-\tau_{ji}(t)))].\end{aligned} \tag{41}$$

By Assumption 3, $\dot{\tau}_{ji}(t) \leq \dot{\tau}_{\max} < 1$, so $1 - \dot{\tau}_{ji}(t) \geq 1 - \dot{\tau}_{\max} > 0$. Combined with the event-triggered condition (15) ($\|\boldsymbol{e}_{\eta,j}^s(t)\|^2 \leq \sigma_j(t)$) and the boundedness of $\dot{\boldsymbol{\eta}}_j(t)$ (derived from system dynamics), $\dot{\mathcal{V}}_{i4}(t)$ can be bounded by a constant and negative terms involving past states (which do not affect the ultimate boundedness).

Synthesis of Stability Results

Combining the derivatives of all four components and applying Young's inequality to all remaining cross terms, this paper can finally obtain the following inequality:

$$\dot{\mathcal{V}}(t) \leq -\kappa\mathcal{V}(t) + \delta, \tag{42}$$

where $\kappa > 0$ is a positive constant dependent on control gains (e.g., $\boldsymbol{K}_{s,i}$, $\boldsymbol{K}_{r,i}$) and adaptive parameters (e.g., $\boldsymbol{\Gamma}_{\Lambda,i}$, $\boldsymbol{\Gamma}_{W,i}$), which can be made sufficiently large by selecting appropriate design parameters. $\delta > 0$ is a positive constant determined by the upper bounds of RBFNN approximation errors ($\varepsilon_{i,\max}$), σ-modification terms, and communication delays.

According to Lyapunov stability theory, if Equation (40) holds, then $\mathcal{V}(t)$ will converge to a compact set $\Omega_{\mathcal{V}} = \{\mathcal{V}(t) \mid \mathcal{V}(t) \leq \delta/\kappa\}$ as $t \to \infty$. Since $\mathcal{V}(t)$ is a quadratic function of all error signals (including $\boldsymbol{s}_i(t)$, $\tilde{\boldsymbol{\Lambda}}_i(t)$, $\tilde{\mathbf{W}}_i(t)$, and $\sigma_i(t)$), the boundedness of $\mathcal{V}(t)$ implies the boundedness of all these signals. Furthermore, by the definition of the sliding mode surface (17) ($\boldsymbol{s}_i(t) = \boldsymbol{e}_{v,i}(t) + \boldsymbol{K}_i\boldsymbol{e}_{\eta,i}(t)$), the boundedness of $\boldsymbol{s}_i(t)$ and $\boldsymbol{e}_{v,i}(t)$ ensures that the formation tracking error $\boldsymbol{e}_{\eta,i}(t)$ is also uniformly ultimately bounded.

The radius of the final error set can be arbitrarily reduced by adjusting design parameters: for example, increasing the control gains $\boldsymbol{K}_{s,i}$ and $\boldsymbol{K}_{r,i}$ or adaptive learning rates $\boldsymbol{\Gamma}_{\Lambda,i}$ and $\boldsymbol{\Gamma}_{W,i}$ will increase κ, thereby decreasing the bound δ/κ. The semi-global property stems from the fact that RBFNN can only guarantee approximation accuracy on compact sets; thus, this stability conclusion holds for any given set of bounded initial conditions. □

4. Simulation

To validate the effectiveness and robustness of the distributed adaptive fault-tolerant formation control algorithm proposed in this paper in handling complex issues such as heterogeneity, communication constraints, actuator faults, and time delays, this chapter conducts numerical simulation experiments. The simulation experiments were completed on a device equipped with a 2.6 GHz Intel Core i7-8750H processor (6 CPU cores), running a Windows 11 64-bit operating system, with the algorithm implemented in MATLAB R2023a.

4.1. Conditions

(1) Formation System Configuration

- Platform Composition: The formation consists of one leader USV (v_0), two follower USVs (v_1, v_2), and three follower AUVs (v_3, v_4, v_5). The USVs use a 3-degree-of-freedom (surge, sway, yaw) dynamic model, while the AUVs use a 6-degree-of-freedom dynamic model. Their specific dynamic parameters, including mass, inertia matrix, and hydrodynamic coefficients, are set based on typical values from the reference [29].
- Environment Setting: The simulation is conducted in a 2 km × 2 km × 0.5 km three-dimensional marine space. To simulate a realistic environment, a constant ocean current with a velocity of 0.3 m/s along the positive X-axis is introduced as an external disturbance term $d_i(t)$ for all platforms.
- Initial State: The initial positions and velocities of all follower platforms are randomly set near the leader's initial position to simulate a non-ideal initial deployment state.

(2) Formation Task Setting

- Leader's Trajectory: The leader USV v_0 sails along a predefined sinusoidal trajectory. Its position in the inertial frame is given by the following equation:

$$\mathbf{x}_0(t) = [3t, 20\sin(0.1t), 0]^T. \tag{43}$$

  This trajectory simulates a common reciprocating survey path.
- Desired Formation: All followers are required to maintain a fixed pentagonal formation relative to the leader. The desired relative position vectors h_i for each follower are set as follows:

$$\begin{cases} h_1 = [-50, 50, 0]^T & (\text{USV } v_1), \\ h_2 = [-50, -50, 0]^T & (\text{USV } v_2), \\ h_3 = [-100, 75, -20]^T & (\text{AUV } v_3), \\ h_4 = [-150, 0, -20]^T & (\text{AUV } v_4), \\ h_5 = [-100, -75, -20]^T & (\text{AUV } v_5). \end{cases} \tag{44}$$

  This formation requires the USVs to accompany on the surface, while the AUVs maintain a wider formation at a depth of 20 m, simulating a typical cross-domain collaborative operation scenario.

(3) Communication and Fault Settings
The basic communication topology of the formation is fully connected. At each time step, each communication link has a probability $p = 0.8$ of remaining connected and a probability $1 - p = 0.2$ of disconnecting, thereby simulating a dynamically changing communication topology. All topologies are assumed to satisfy Assumption 1.

To simulate the differences in communication methods, the time delays are set as follows: the time-varying delay for electromagnetic communication between USVs is $\tau_{ij}(t) \in [0.1, 0.3]$ s; the time-varying delay for underwater acoustic communication between USVs and AUVs is $\tau_{ij}(t) \in [0.8, 1.2]$ s.

To test the fault-tolerant performance of the controller, two typical actuator faults are introduced during the simulation:

(a) **Effectiveness Fault:** At $t = 300$ s, a 25% loss of effectiveness, a fault is injected into the main thruster of USV v_2, meaning its effectiveness factor ρ_2 abruptly changes from 1 to 0.75.

(b) **Bias Fault:** At $t = 500$ s, a persistent bias fault b_4 of magnitude $5\,N \cdot m$ is injected into the vertical rudder of AUV v_4.

(4) Controller Parameter Settings

(a) Sliding mode surface parameters: $\lambda_i = \text{diag}\{1.5, 1.5, \dots\}$ for all $i \in \mathcal{F}$.
(b) Sliding mode control gains: $K_{s,i} = \text{diag}\{10, 10, \dots\}$, $K_{d,i} = \text{diag}\{0.5, 0.5, \dots\}$.
(c) Adaptive law gains: $\Gamma_{W,i} = \text{diag}\{5, 5, \dots\}$, $\gamma_{\rho,ij} = 0.8$, $\sigma_{W,i} = \sigma_{\rho,ij} = 0.01$.
(d) Dynamic event-triggering parameters: $k_{\eta,1} = 0.5$, $k_{\eta,2} = 1.0$, $\sigma_\eta = 5.0$.
(e) Boundary layer thickness: $\epsilon = 0.5$.
(f) RBF Neural Network: Each follower's controller uses an RBFNN to approximate the unknown nonlinear terms. Each RBFNN contains 20 neurons, with their centers uniformly distributed within the expected range of the input variables, and the width is uniformly set to 2, as shown in Figure 3.

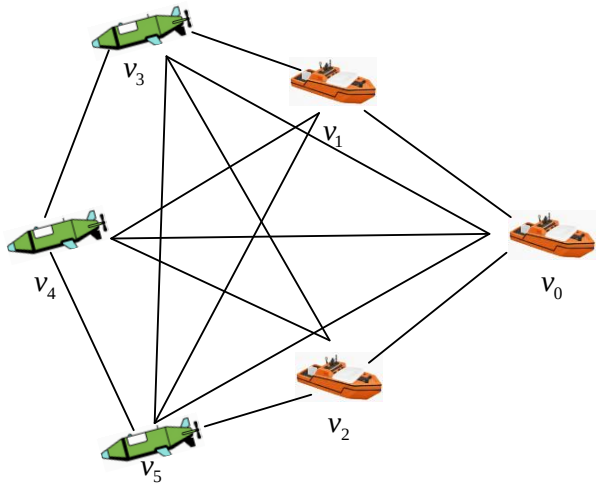

Figure 3. Formation topology structure.

4.2. Results

4.2.1. Formation Tracking Performance

Figure 4 shows the motion trajectories of the entire heterogeneous formation in 3D space and on a 2D plane, respectively. The leader USV (red solid line) accurately follows the preset sinusoidal path. It can be visually observed from the figures that although all followers start from random initial positions, they can quickly converge to the desired pentagonal formation centered on the leader. The two follower USVs (blue dashed lines) successfully form the inner formation on the water surface (Z = 0), while the three follower AUVs (green dash-dotted lines) form the outer formation at a depth of 20 m. Macroscopically, the entire pentagonal formation configuration is well maintained throughout the mission and follows the leader as a whole, visually verifying the effectiveness of the algorithm.

Figure 5 compares the positions of all platforms along the X, Y, and Z axes. It can be seen that the position curves of all followers maintain the desired offset from the leader's curve, showing good consistency. Particularly in the Z-axis subplot, it is clearly shown that the AUV cluster successfully maintains the target depth of -20 m, while the USVs remain on the water surface.

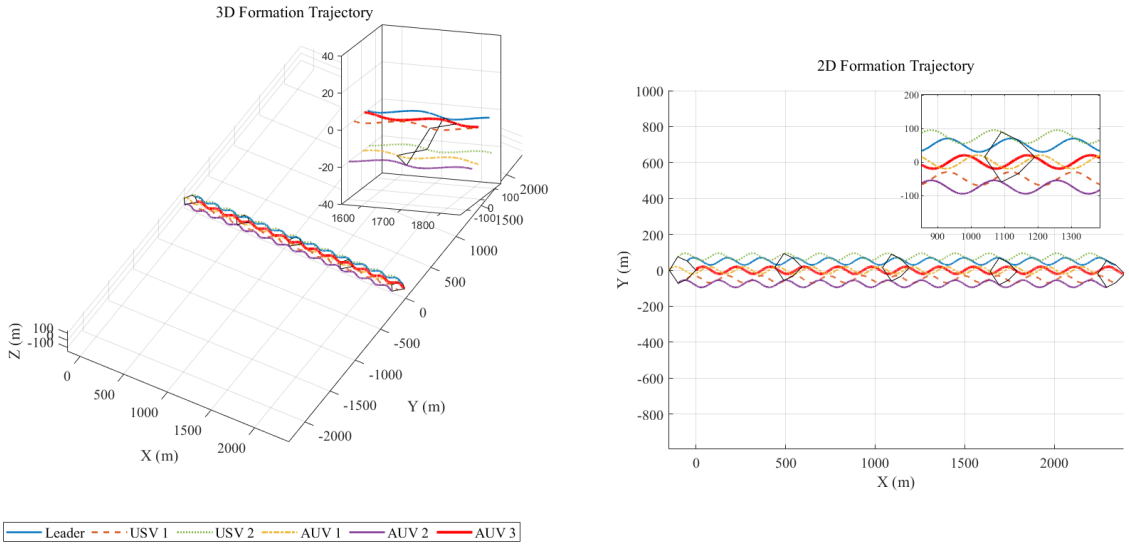

Figure 4. Overview of the USV–AUV formation trajectory. The 3D view (**left**) illustrates the overall convergence of the heterogeneous swarm from random initial positions to the desired pentagonal formation. The 2D view (**top-right**, with zoomed inset) explicitly shows the leader's (red) sinusoidal path in the X-Y plane and the followers successfully maintaining their predefined offsets.

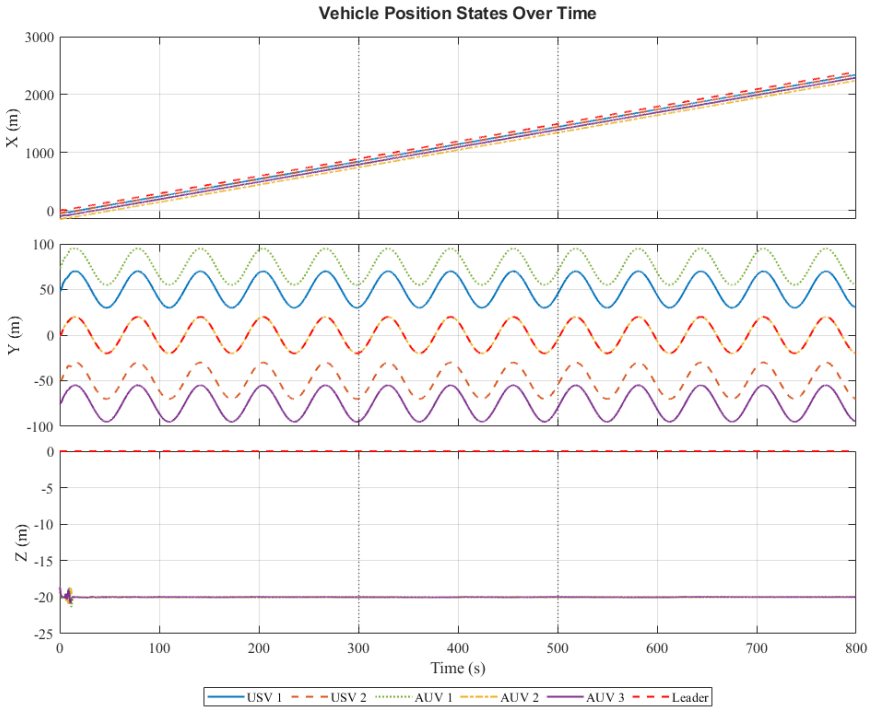

Figure 5. Vehicle position states over time, demonstrating formation geometry maintenance. The **top** plot (X axis) shows all agents tracking the leader's ramp trajectory. The **middle** plot (Y axis) confirms the sinusoidal offsets are maintained relative to the leader (red). The **bottom** plot (Z axis) validates the system's heterogeneity handling, with USVs (blue, orange) remaining at the surface ($Z = 0$) and AUVs (green, yellow, purple) correctly maintaining the -20 m target depth.

The first figure in Figure 6 shows that the speeds of all followers quickly converge and closely track the leader's speed curve after the initial phase. The heading/yaw angle comparison in the first figure in Figure 6 also shows a high degree of consistency. The first figure in Figure 6 indicates that the pitch angles of the AUVs remain within a small range of fluctuation around zero throughout the mission, demonstrating stable attitude.

Figure 7 presents the time response curves of the position tracking error norm for each follower. The tracking errors of all followers rapidly converge to a very small neighborhood within the initial phase (approximately 50 s), indicating that the system has good transient performance. At $t = 300$ s (fault) and $t = 500$ s (fault), the errors of the corresponding unmanned platforms show brief, minor peaks, but are quickly suppressed by the adaptive fault-tolerant controller and return to a stable state. Similarly, when the topology switches, the error shows strong robustness with almost no fluctuation. This strongly demonstrates the robustness of the controller to actuator faults and network topology changes, as well as the uniformly ultimately bounded nature of the system error.

The performance of the controller is evaluated using several key metrics, summarized in Table 2. The Root Mean Square Error (RMSE) and Mean Absolute Error (MAE) are calculated for the formation tracking error norm $||e_{\eta,i}(t)||$ during the steady-state period ($t = 100$ s to 800 s).

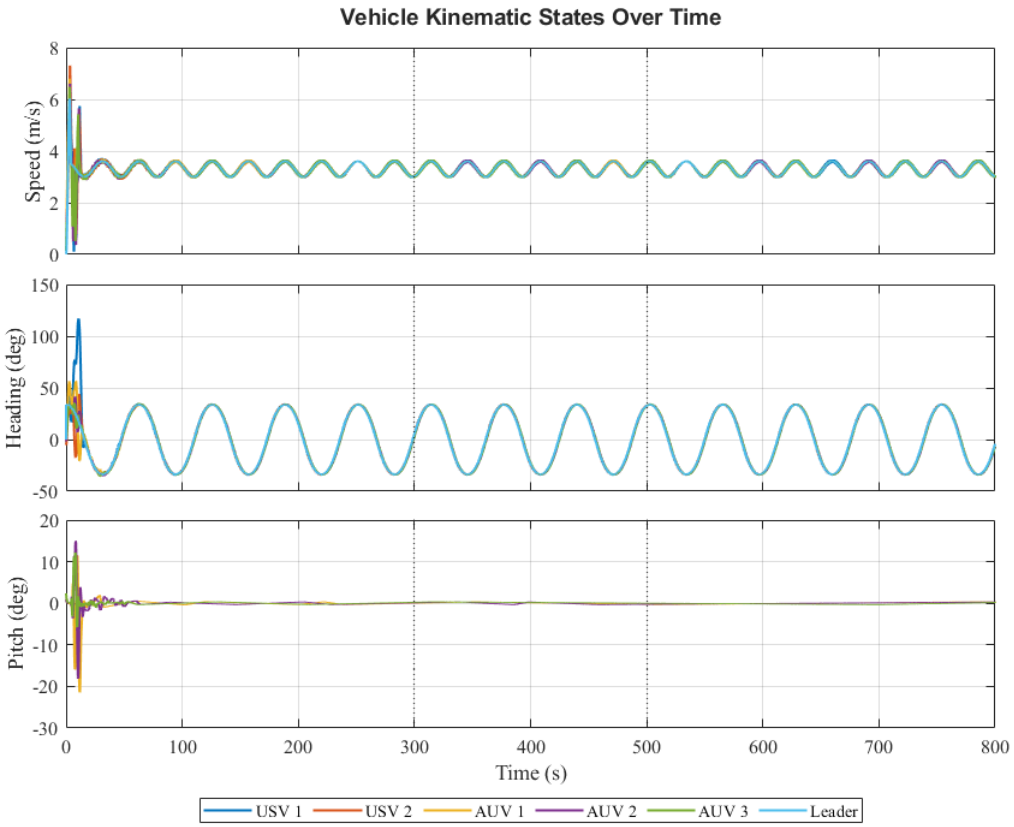

Figure 6. Kinematic state tracking performance. (**Top**) Follower speeds converge rapidly (within approx. 50 s) to the leader's time varying speed. (**Middle**) Follower headings (yaw) align and track the leader's heading changes. (**Bottom**) AUV pitch angles are stabilized near zero, indicating good attitude control during 3D maneuvering.

Table 2. Quantitative Performance Analysis of Followers.

Metric	USV 1	USV 2	AUV 1	AUV 2	AUV 3
RMSE (m)	0.09	0.14	0.12	0.13	0.12
MAE (m)	0.07	0.11	0.09	0.10	0.09
Total Triggers (800 s)	28	33	30	34	29
Avg. Trigger Interval (s)	28.5	24.2	26.7	23.5	27.6

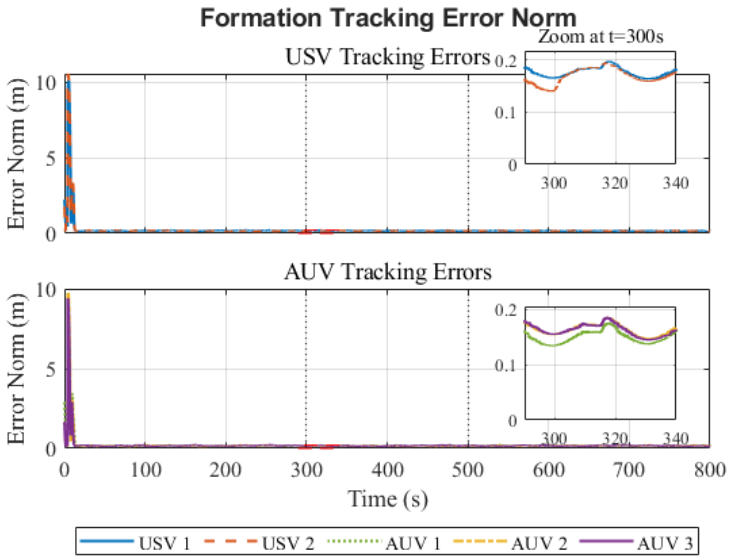

Figure 7. Formation tracking error norm ($||e_{\eta,i}(t)||$). This plot demonstrates the controller's robustness and SGUUB performance. The error for all followers converges to a small compact set (<0.2 m) within approximately 50 s. The insets highlight the system's fault-tolerant capability: at $t = 300$ s (USV 2 fault) and $t = 500$ s (AUV 4 fault, not shown in USV plot), only minor, brief error spikes (peaking below 0.2 m) occur before being quickly suppressed by the adaptive controller.

The results in Table 2 quantify the visual findings from Figure 7. The steady-state RMSE and MAE are consistently low (on the order of ∼0.1 m), confirming high tracking accuracy. For USV 2 and AUV 2 (which experienced faults at t = 300 s and t = 500 s, respectively, corresponding to AUV 4 in the setup), the maximum error variation during the fault event remained small (0.19 m and 0.18 m), demonstrating the controller's rapid fault suppression capability.

Furthermore, the communication performance is notable. The average time between communication triggers for the fleet is approximately 26.0 s. Compared to a typical periodic control update (e.g., 10 Hz, or 0.1 s interval), which would require 8000 triggers per agent, the proposed DETM (averaging ∼31 triggers) achieves a communication load reduction of approximately 99.6% (calculated as $1 - (31/8000)$). This validates the significant efficiency of the proposed mechanism.

4.2.2. Communication Efficiency Analysis

The event-triggering interval plot (Figure 8) intuitively demonstrates the effectiveness of the DETM. In the initial stage of the simulation, the triggering interval is small (frequent communication) due to large errors. Once the system stabilizes, the triggering interval significantly increases to several seconds, greatly reducing the communication frequency. At the moment a fault occurs, the triggering interval of the corresponding platform briefly decreases to cope with the sudden situation, reflecting the adaptiveness of the mechanism.

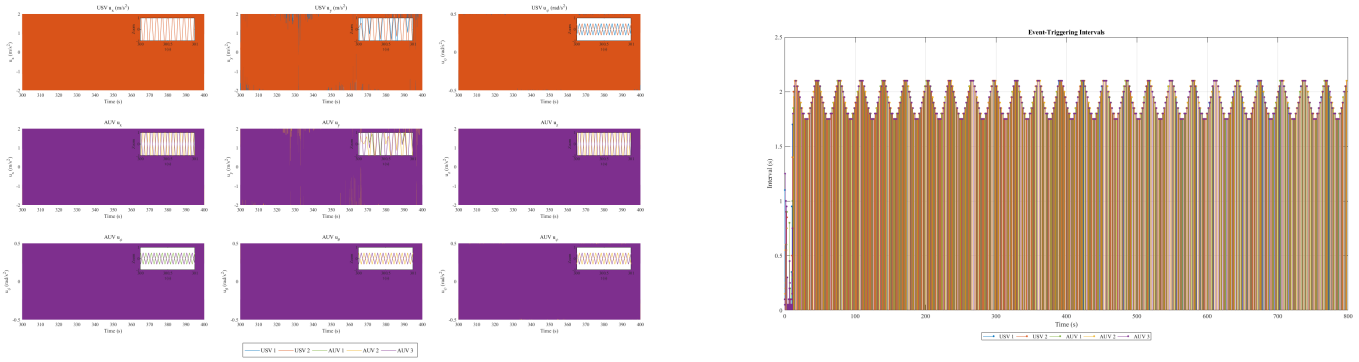

(**a**) (**b**)

Figure 8. Event triggered simulation diagram. (**a**) Control inputs (**b**) Event-triggering intervals. Plot (**b**) validates the efficiency of the DETM. The communication intervals are short (e.g., <5 s) during the initial high-error transient phase. Once the system stabilizes (error is low), the intervals increase significantly (up to 30 s+), drastically reducing communication load. Note that intervals briefly shorten at $t = 300$ s and $t = 500$ s to provide more data precisely when faults occur, demonstrating the mechanism's dynamic adaptiveness.

4.2.3. Adaptive and Fault-Tolerant Capability Analysis

Figure 9 plots the norm of the adaptive bias estimate $\|\hat{b}_i\|$. It can be seen that for healthy platforms, this estimate remains close to zero. When USV 2 experiences a fault at $t = 300$ s, its $\|\hat{b}_2\|$ rapidly increases and converges to a stable value, accurately learning the fault bias. Similarly, when AUV 4 experiences a fault at $t = 500$ s, its $\|\hat{b}_4\|$ shows the same correct response. This proves that the adaptive law can accurately identify and compensate for unknown bias faults online.

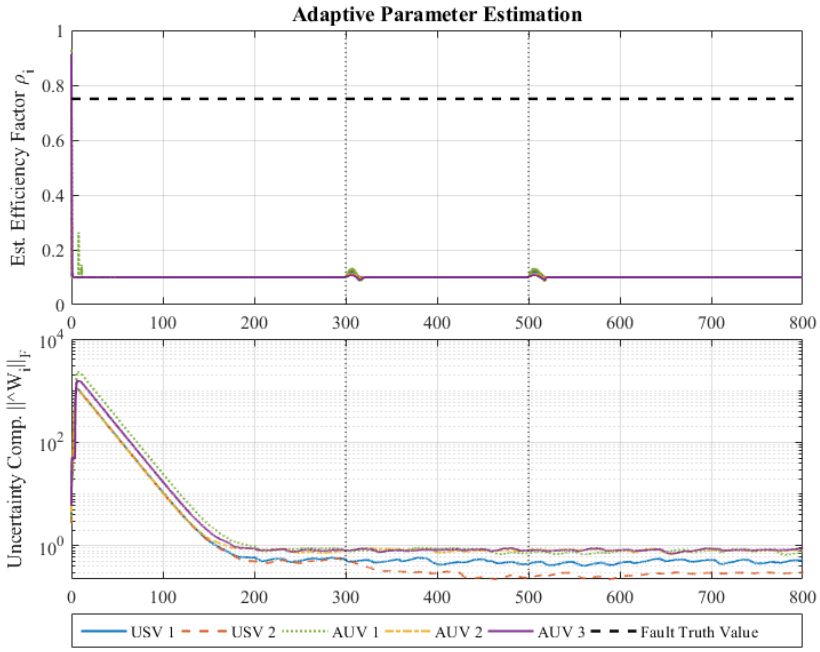

Figure 9. Performance of the adaptive fault-tolerant estimators. (**Top**) The estimated efficiency factor for USV 2 (orange) correctly identifies the fault at $t = 300$ s, with its estimate dropping from 1.0 toward the true fault value (0.75, black dashed line). (**Bottom**) The norm of the RBFNN weight estimate ($||\hat{W}_i||$), which compensates for both unmodeled dynamics and bias faults. Note the clear step-change for AUV 4 (yellow) at $t = 500$ s as its RBFNN learns to compensate for the newly injected bias fault.

The results comprehensively verify the effectiveness of the proposed distributed adaptive fault-tolerant control scheme from multiple perspectives. The scheme can be successfully applied to a simplified heterogeneous USV-AUV system, ensuring high-precision formation tracking while effectively handling challenges such as actuator bias faults and communication topology switching, and significantly improving communication efficiency, demonstrating its potential for practical application.

5. Conclusions

This paper proposed a DAFTC framework for heterogeneous USV-AUV formations operating under communication delays, time-varying topologies, and actuator faults. The core novelty of the DAFTC framework lies in its cohesive integration of a DETM with an RBFNN-based adaptive fault-tolerant strategy. This synergy provides a robust and communication-efficient solution, where the DETM dynamically saves the network bandwidth (validated by a >99.6% reduction in simulation) while the adaptive laws actively compensate for internal faults (effectiveness loss and bias), ensuring formation stability (RMSE < 0.15 m) even under uncertainty.

The practical significance of this framework is its direct applicability to multi-domain marine cooperation. By unifying the heterogeneous Euler–Lagrange dynamics and rigorously handling the high-latency, unreliable nature of underwater acoustic/radio links via Lyapunov–Krasovskii analysis, this work provides a stable control backbone essential for complex real-world tasks like coordinated surveys or monitoring.

Despite these results, the proposed model has limitations. The current framework relies on the assumption that the leader's state is accessible to at least one follower (Assumption 1) and that faults, while unknown, are bounded (Assumption 2). Furthermore, the RBFNN approximator, while effective, adds computational complexity that must be considered for implementation on embedded systems.

The extendibility of this work to real-world platforms is a key future direction. Future research will focus on (1) integrating collision avoidance strategies to handle dynamic obstacles; (2) enhancing the model to address sudden shock disturbances for improved load compensation capability; (3) applying the control scheme to high-fidelity nonlinear hydrodynamic models rather than the simplified model; and (4) performing verification on physical USV-AUV hardware platforms.

Author Contributions: Conceptualization, H.W. (Haitao Wang); Methodology, H.W. (Haitao Wang); Software, H.W. (Hanyi Wang); Validation, H.W. (Haitao Wang); Formal analysis, H.W. (Haitao Wang); Investigation, H.W. (Haitao Wang) and X.G.; Resources, H.W. (Hanyi Wang); Data curation, H.W. (Haitao Wang); Writing—original draft, H.W. (Hanyi Wang); Writing—review & editing, H.W. (Hanyi Wang) and X.G.; Visualization, H.W. (Haitao Wang); Supervision, X.G. All authors have read and agreed to the published version of the manuscript.

Funding: This research received no external funding.

Data Availability Statement: The original contributions presented in this study are included in the article. Further inquiries can be directed to the corresponding author.

Conflicts of Interest: The authors declare no conflicts of interest.

References

1. Li, J.; Zhang, G.; Zhang, W.; Shan, Q.; Zhang, W. Cooperative path following control of USV-UAVs considering low design complexity and command transmission requirements. *IEEE Trans. Intell. Veh.* **2023**, *9*, 715–724. [CrossRef]
2. Zhang, J.; Ren, J.; Cui, Y.; Fu, D.; Cong, J. Multi-USV task planning method based on improved deep reinforcement learning. *IEEE Internet Things J.* **2024**, *11*, 18549–18567. [CrossRef]
3. Xu, D.; Yang, J.; Zhou, X.; Xu, H. Hybrid path planning method for USV using bidirectional A* and improved DWA considering the manoeuvrability and COLREGs. *Ocean Eng.* **2024**, *298*, 117210. [CrossRef]
4. Li, J.; Xiang, X.; Zhang, Q.; Yang, S. Robust practical prescribed time trajectory tracking of USV with guaranteed performance. *Ocean Eng.* **2024**, *302*, 117622. [CrossRef]
5. Wang, L.; Zhu, D.; Pang, W.; Zhang, Y. A survey of underwater search for multi-target using Multi-AUV: Task allocation, path planning, and formation control. *Ocean Eng.* **2023**, *278*, 114393. [CrossRef]
6. Wang, Y.; Li, H.P.; Yao, Y. An adaptive distributed auction algorithm and its application to multi-AUV task assignment. *Sci. China Technol. Sci.* **2023**, *66*, 1235–1244. [CrossRef]
7. Chen, Z.; Zhang, D.; Wang, C.; Sha, Q. Hybrid form of differential evolutionary and gray wolf algorithm for multi-auv task allocation in target search. *Electronics* **2023**, *12*, 4575. [CrossRef]
8. Zhang, M.; Chen, H.; Cai, W. Hunting task allocation for heterogeneous multi-AUV formation target hunting in IoUT: A game theoretic approach. *IEEE Internet Things J.* **2023**, *11*, 9142–9152. [CrossRef]
9. Zhang, H.; Wang, H.; Lei, J.; Zhao, W. Improved analytical solution with optimization constraints using TDOA and FDOA measurements for USV/AUV collaborative localization. *Signal Process.* **2025**, *228*, 109760. [CrossRef]
10. Wang, Z.; Xu, J.; Feng, Y.; Wang, Y.; Xie, G.; Hou, X.; Men, W.; Ren, Y. Fisher-information-matrix-based usbl cooperative location in usv–auv networks. *Sensors* **2023**, *23*, 7429. [CrossRef]
11. Hu, R.; Wu, D.; You, Z.; Wu, D.; Tu, W. Predefined-time terminal sliding mode cooperative trajectory tracking control for USV-AUV under weak communication. *Ocean Eng.* **2025**, *333*, 121459. [CrossRef]
12. Guo, X.; Li, Q.; Yao, Q.; Lu, X. Distributed fixed-time sliding mode formation control for unmanned aerial-ground vehicle (UAV-UGV) heterogeneous system. *Asian J. Control* **2025**, *27*, 1802–1816. [CrossRef]
13. Zhu, Y.; Li, S.; Guo, G.; Yuan, P.; Bai, J. Formation control of UAV–USV based on distributed event-triggered adaptive MPC with virtual trajectory restriction. *Ocean Eng.* **2024**, *294*, 116850. [CrossRef]
14. Wu, L.F.; Rastgaar, M.; Mahmoudian, N. Heterogeneous Multi-Robot (UAV-USV-AUV) Collaborative Exploration with Energy Replenishment. *IFAC-PapersOnLine* **2024**, *58*, 159–164. [CrossRef]
15. Li, C.; Li, J.; Zhang, G.; Chen, T. IROA-based LDPC-Lévy method for target search of multi AUV–USV system in unknown 3D environment. *Ocean Eng.* **2023**, *286*, 115648. [CrossRef]
16. Jia, Z.; Lu, H.; Li, S.; Zhang, W. Distributed dynamic rendezvous control of the AUV-USV joint system with practical disturbance compensations using model predictive control. *Ocean Eng.* **2022**, *258*, 111268. [CrossRef]
17. Yang, Y.; Zhang, J.; Huang, M.; Tan, X. Disturbance observer-based event-triggered control of switched positive systems. *IEEE Trans. Circuits Syst. II Exp. Briefs* **2023**, *71*, 1191–1195. [CrossRef]
18. Xu, T.; Sun, Z.; Wen, G.; Duan, Z. Data-driven dynamic event-triggered control. *IEEE Trans. Autom. Control* **2024**, *69*, 8804–8811. [CrossRef]
19. Wang, Z.; Chadli M. Observer-based distributed dynamic event-triggered control of multi-agent systems with adjustable interevent time. *Asian J. Control* **2024**, *26*, 2783–2795. [CrossRef]
20. Sewlia, M.; Zelazo, D. Bearing-based formation stabilization using event-triggered control. *Int. J. Robust Nonlinear Control* **2024**, *34*, 4375–4387. [CrossRef]
21. Wang, M.; Chen, J.; Wen, C.; Qin, S. Adaptive generalized nash equilibrium seeking algorithm for nonsmooth aggregative game under dynamic event-triggered mechanism. *Automatica* **2024**, *169*, 111835. [CrossRef]
22. Yuan, Y.; He, W.; Du, W.; Tian, Y.-C.; Han, Q.-L.; Qian, F. Distributed gradient tracking for differentially private multi-agent optimization with a dynamic event-triggered mechanism. *IEEE Trans. Syst. Man Cybern. Syst.* **2024**, *54*, 3044–3055. [CrossRef]
23. Xu, T.; Duan, Z.; Wen, G.; Sun, Z. A novel dynamic event-triggered mechanism for dynamic average consensus. *Automatica* **2024**, *161*, 111495. [CrossRef]
24. Zhang, K.; He, W.; Xu, W. Dynamic event-triggered mechanism for distributed Nash equilibrium seeking under switching topologies. *IEEE Trans. Ind. Inform.* 2024, *in press*. [CrossRef]
25. Guo, Y.; Wang, Q.; Sun, P.; Feng, X. Distributed adaptive fault-tolerant control for high-speed trains using multi-agent system model. *IEEE Trans. Veh. Technol.* **2023**, *73*, 3277–3286. [CrossRef]
26. Lu, L.T.; Zhu, S.L.; Wang, D.M.; Han, Y.Q. Distributed adaptive fault-tolerant control with prescribed performance for nonlinear multiagent systems. *Commun. Nonlinear Sci. Numer. Simul.* **2024**, *138*, 108222. [CrossRef]

27. Yu, Z.; Zhou, R.; Sun, P.; Zhang, Y.; Jiang, B.; Su, C.-Y. Hierarchical distributed adaptive fault-tolerant control of nonlinear fractional-order multiagent systems with faults and periodic disturbances using event-triggered communication. *IEEE Trans. Cybern.* **2024**, *54*, 5231–5243. [CrossRef]
28. Deng, C.; Yang, G.H. Distributed adaptive fault-tolerant control approach to cooperative output regulation for linear multi-agent systems. *Automatica* **2019**, *103*, 62–68. [CrossRef]
29. Perez, T.; Fossen, T.I. Kinematic models for manoeuvring and seakeeping of marine vessels. *Model. Identif. Control* **2007**, *28*, 19. [CrossRef]